

## Article

# Paleoenvironmental Transition during the Rhuddanian–Aeronian and Its Implications for Lithofacies Evolution and Shale Gas Exploration: Insights from the Changning Area, Southern Sichuan Basin, South-West China

Hangyi Zhu

Research Institute of Petroleum Exploration and Development, PetroChina, Beijing 100083, China; zzzshalegas@cnpc.com.cn

**Abstract:** During the Rhuddanian–Aeronian interglacial period, global geological events such as glacial melting, synsedimentary volcanic activity, biological resurgence, and large-scale marine transgressions caused frequent fluctuations in paleoproductivity, climate changes, and sea level variations. These paleoenvironmental transitions directly influenced the development characteristics of shale lithofacies. This study investigates the Longmaxi Formation shale in the Changning area in the Southern Sichuan basin, focusing on 28 core samples from Well N1. Using scanning electron microscopy, QEMSCAN, TOC, XRD, and major and trace element analyses, we reconstructed the paleoenvironmental transitions of this period and explored their control over shale lithofacies types and mineral compositions. Four shale lithofacies were identified: carbonate rich lithofacies (CRF), biogenic quartz-rich lithofacies (BQRF), detrital clay-rich lithofacies (CRDF), and detrital quartz-rich lithofacies (DQRF). During the Rhuddanian period, rising global temperatures caused glacial melting and rapid marine transgressions. The low oxygen levels in bottom waters, combined with upwelling and abundant volcanic material, led to high paleoproductivity. This period primarily developed BQRF and CRF. Rich nutrients and abundant siliceous organisms, along with anoxic to anaerobic conditions, provided the material basis and preservation conditions for high biogenic quartz and organic matter content. High paleoproductivity and anoxic conditions also facilitated the precipitation of synsedimentary calcite and supplied  $Mg^{2+}$  and  $SO_4^{2-}$  for the formation of iron-poor dolomite via sulfate reduction. From the Late Rhuddanian to the Mid-Aeronian, the Guangxi orogeny caused sea levels to fall, increasing water oxidation and reducing upwelling and volcanic activity, which lowered paleoproductivity. Rapid sedimentation rates, stepwise global temperature increases, and the intermittent intensification of weathering affected terrigenous clastic input, resulting in the alternating deposition of CRF, CRDF, and DQRF. Two favorable shale gas reservoirs were identified from the Rhuddanian–Aeronian period: Type I (BQRF) in the L1–L3 Layers, characterized by high TOC and brittleness, and Type II (DQRF) in the L4 Layer, with significant detrital quartz content. The Type I-favorable reservoir supports ongoing gas production, and the Type II-favorable reservoir offers potential as a future exploration target.



**Citation:** Zhu, H. Paleoenvironmental Transition during the Rhuddanian–Aeronian and Its Implications for Lithofacies Evolution and Shale Gas Exploration: Insights from the Changning Area, Southern Sichuan Basin, South-West China. *Minerals* **2024**, *14*, 949. <https://doi.org/10.3390/min14090949>

Academic Editors: Marianna Kulkova and Dmitry Subetto

Received: 16 July 2024

Revised: 4 September 2024

Accepted: 16 September 2024

Published: 18 September 2024

**Keywords:** Rhuddanian–Aeronian stage; paleoenvironment; shale; lithofacies; sea level variation



**Copyright:** © 2024 by the author. Licensee MDPI, Basel, Switzerland. This article is an open access article distributed under the terms and conditions of the Creative Commons Attribution (CC BY) license (<https://creativecommons.org/licenses/by/4.0/>).

## 1. Introduction

During the Late Ordovician to Early Silurian time (455–430 Ma), a series of global geological events occurred, including mass extinctions, the Hirnantian glaciation, rapid global sea-level changes, and marine anoxia events [1–3]. These significant events caused dramatic changes in the paleogeographic environment, which influenced shale mineral composition and organic matter accumulation [1–3]. The large-scale melting of glaciers in the Early Silurian led to significant freshwater input into the ocean, causing a substantial

rise in sea level and the formation of anoxic environments conducive to the preservation of organic matter [4,5]. Moreover, mass extinctions and volcanic ash-induced algal blooms significantly increase paleoproductivity, providing a rich material basis for organic matter accumulation [6–9]. The warming climate has also led to a significant increase in siliceous plankton, such as radiolarians and sponge spicules, which absorb  $\text{Si}^{4+}$  from water and transform it into unstable opal-A during growth, eventually forming a substantial amount of biogenic microcrystalline quartz with increasing burial temperature and pressure [10–13]. High-content biogenic quartz substantially increases reservoir compressive strength, preserving primary porosity [10–13]. Biogenic quartz aggregates not only provide ample storage space for organic matter but also enhance the compressive strength of shale reservoirs, thus protecting primary porosity [14,15]. Consequently, the Early Silurian global transgression resulted in the widespread development of thick, stable, highly brittle, and porous organic-rich shales worldwide, such as in the Southern Uplands of Scotland [16–18], the deep shelf of northern England [19,20], deep shelf basins in Poland ([21], Holy Cross, peri-Baltic, Carpathian), southern Sweden and Bornholm Island [22], Nevada's Vinini Creek [23,24], southeastern Alaska [25,26], northern Yukon in Canada [27–29], South China's Sichuan basin [30–34], the Prague Basin in the Czech Republic [35–37], and the Victoria back-arc basin in Australia [38,39]. Among these, the Longmaxi Formation organic-rich shales in the southern Sichuan basin are characterized by high TOC (2%–7%), significant thicknesses (30–40 m), good reservoir properties (porosity 2%–8%), and high gas contents. This formation is the only shale layer in China that has achieved commercial shale gas development [40–42]. The enrichment of shale gas depends on the accumulation of organic matter and the mineral composition of the reservoir, with the TOC content determining the gas generation potential and mineral composition directly controlling the reservoir properties and brittleness [9,41–43]. Therefore, studying the paleoenvironmental changes in the Early Silurian provides a theoretical basis and guidance for exploring the distribution patterns of organic-rich shales and evaluating the conditions for shale gas enrichment.

The Longmaxi Formation organic-rich shale exhibits significant heterogeneity in mineral composition, sedimentary structure, chemical elements, and organic matter enrichment, which is reflected in the frequent changes in lithofacies types [44–46]. Global geological events, such as frequent volcanic activity, the end of the Hirnantian glaciation, the development of upwelling currents, and mass extinctions, collectively caused shifts in the paleoenvironment and sedimentary processes during the Early Silurian, leading to rapid lithofacies changes [46,47]. Scholars generally believe that the main controlling factors of Early Silurian shale lithofacies include (1) the suspension sedimentation process of fine-grained sediments [44,45], (2) high paleoproductivity [44,46,48], (3) anoxic bottom water conditions [45,47,48], (4) secondary sea-level rises [3,49], (5) low terrigenous clastic input [50,51], (6) cold and dry paleoclimate [8,49], and (7) the coupling of various depositional events, such as turbidite and bottom current deposits [47,52]. However, these individual paleoenvironmental factors alone cannot fully explain the processes and mechanisms of lithofacies changes. Clarifying the relationships among paleoproductivity, redox conditions, terrigenous clastic input, paleoclimate, and the coupling of depositional events is crucial for understanding lithofacies development in the lower Silurian.

Furthermore, current research predominantly focuses on the transition period from the Late Ordovician to the Early Silurian, especially the influence of paleoenvironmental changes on organic matter accumulation mechanisms and lithofacies development during the Hirnantian and Rhuddanian stages [1,5,40,41,52]. Research on how paleoenvironmental changes during the Rhuddanian to Aeronian stages influenced lithofacies development is limited, with the effects of small-scale transgressive events often being overlooked [6–12]. Numerous studies have validated that organic-rich and biogenic quartz-rich shales formed under rapid transgression during the Early Rhuddanian (which is widely called the “L1 Layer”) and can serve as significant targets for shale gas exploration and development in the southern Sichuan basin (hereinafter referred to as “southern Sichuan”). The L1 Layer

achieved a state appropriate for commercial development in the Early Rhuddanian [7–9]. However, the current recovery rate of shale gas from the Early Silurian is only 23.4% to 24.8%. This low recovery rate indicates that relying solely on a thin, 1–5 m, shale gas layer from the Early Rhuddanian stage is insufficient for effective exploration and development [4,7,8]. Moreover, understanding whether the frequent, small-scale sea level rises during the Rhuddanian–Aeronian period could have controlled the large-scale formation of organic-rich shale lithofacies is crucial for identifying potential successor layers to the L1 Layer. To ensure stable shale gas production in mature blocks from the Early Silurian, it is essential to identify whether other favorable shale gas layers or organic-rich lithofacies, such as the replacement interval of the L1 Layer during the Rhuddanian–Aeronian period, are present in the lower Silurian strata. This identification is crucial for enhancing recovery rates, supporting integrated development, and evaluating resource potential while discovering new prospective exploration areas.

To address these issues, this study collected 28 marine shale samples from the Longmaxi Formation in Well N1 of the Changning area, southern Sichuan, for lithofacies analysis, TOC testing, mineral content testing, and major and trace element analysis. We analyzed the paleoenvironmental changes from the Rhuddanian to Aeronian stages in the Changning area and explored the control of these paleoenvironmental changes on lithofacies development.

## 2. Geological Settings

The South China Block, which includes the Yangtze and Cathaysia plates, was attached to the edge of the Gondwana supercontinent during the Early Silurian [8,9,42,47]. During the Ordovician–Silurian transition, the Yangtze Block experienced the deposition of black shales, the South China Basin disappeared, and the South China orogenic belt formed [9]. After the Late Ordovician, a large-scale orogenic event known as the Guangxi Orogeny occurred along the southeastern margins of the Cathaysia and Yangtze blocks [42,47]. As the Aeronian stage began, the Guangxi Orogeny intensified, accompanied by significant sea-level fluctuations during this period [5]. The South China craton is near the paleoequator within the active tectonic zone of northwestern Gondwana [41]. The Caledonian orogeny was most intense during this time, causing compressional conditions in the Upper Yangtze platform and the formation of several uplifts around the platform, such as the “Central Sichuan uplift” to the northwest, the “Central Guizhou Uplift” to the south, and the Jiangnan-Xuefeng uplift to the southeast [53,54].

During the Late Ordovician to Early Silurian, global sea levels underwent significant fluctuations, resulting in one second-order relative sea-level cycle and four third-order relative sea-level cycles [53,54]. In the Early Silurian, rapid sea-level rise (corresponding to the second-order relative sea-level rise event), combined with the expansion of the Cathaysia Plate and uplift across much of South China, led to substantial changes in the distribution of land and sea in the region [53,54]. At this time, global climate began to warm, ice sheets gradually retreated, marking the onset of a new interglacial period [41]. The resulting restricted paleogeographic configuration created a low-energy, anoxic depositional environment in the Inner Yangtze Sea, leading to the formation of organic-rich Longmaxi Formation shales [53,54].

The study area is located in the southwestern Changning block of southern Sichuan (Figures 1 and 2). All samples for this study were collected from the Longmaxi Formation shale cores of Well N1 in the Changning block (Figures 1 and 2). This well penetrated a complete and continuous stratigraphic sequence from the Upper Ordovician Baota Formation to the lower Silurian Longmaxi Formation. The Wufeng Formation, deposited during the Katian and Hirnantian stages [55], consists of dark gray to black clay-rich shales and black siliceous shales [53,54]. The overlying Guanyinqiao Bed is composed of bioclastic limestone [55]. The base of the Longmaxi Formation (444.43–438.13 Ma) consists of black siliceous shales, gradually transitioning upward to gray silty shales and siltstones [55]. According to the development of graptolite zones, the Longmaxi Formation is divided into six units from bottom to top [55]: L1 (graptolite zone LM1, *Persculptog. persculptus*), L2

(LM2, LM3 *Akidograptus ascensus*, *Parakidogr. acuminatus*), L3 (LM4, *Cystograptus vesiculosus*), L4 (LM5, *Coronograptus cyphus*), L5 (LM6, *Demirastrites triangulates*), and L6 (LM7–9, *Spirograptus guerichi*, *Stimulograptus sedgwickii*, *Lituigraptus convolutus*).

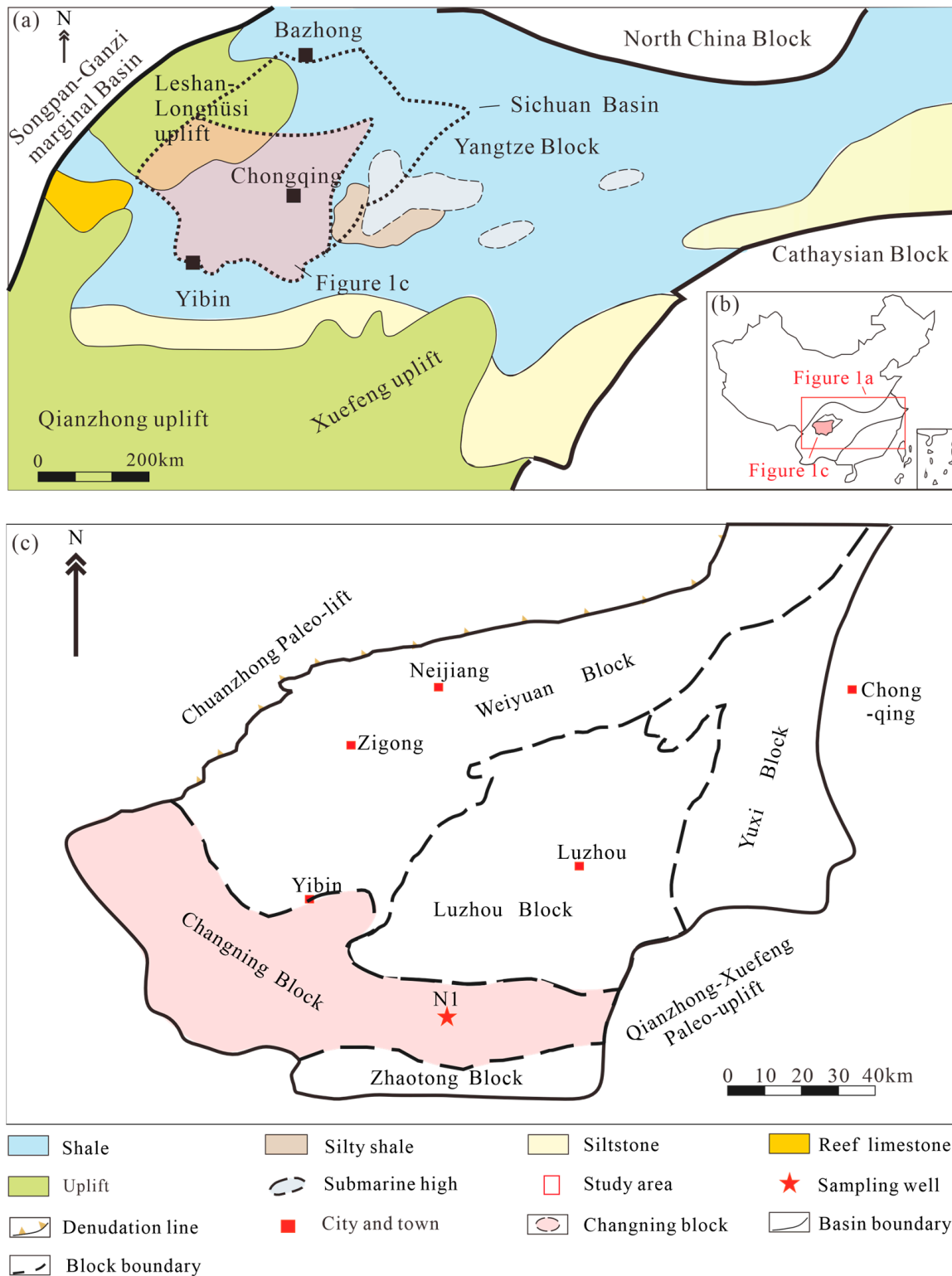


**Figure 1.** (a) The Upper Yangtze platform’s position during the Rhuddanian–Aeronian period, adapted from [53]. (b) Geographical distribution of the Sichuan basin within China, adapted from [8]. (c) The distribution of the research area (Changning Block) in the Sichuan Basin, adapted from [33].

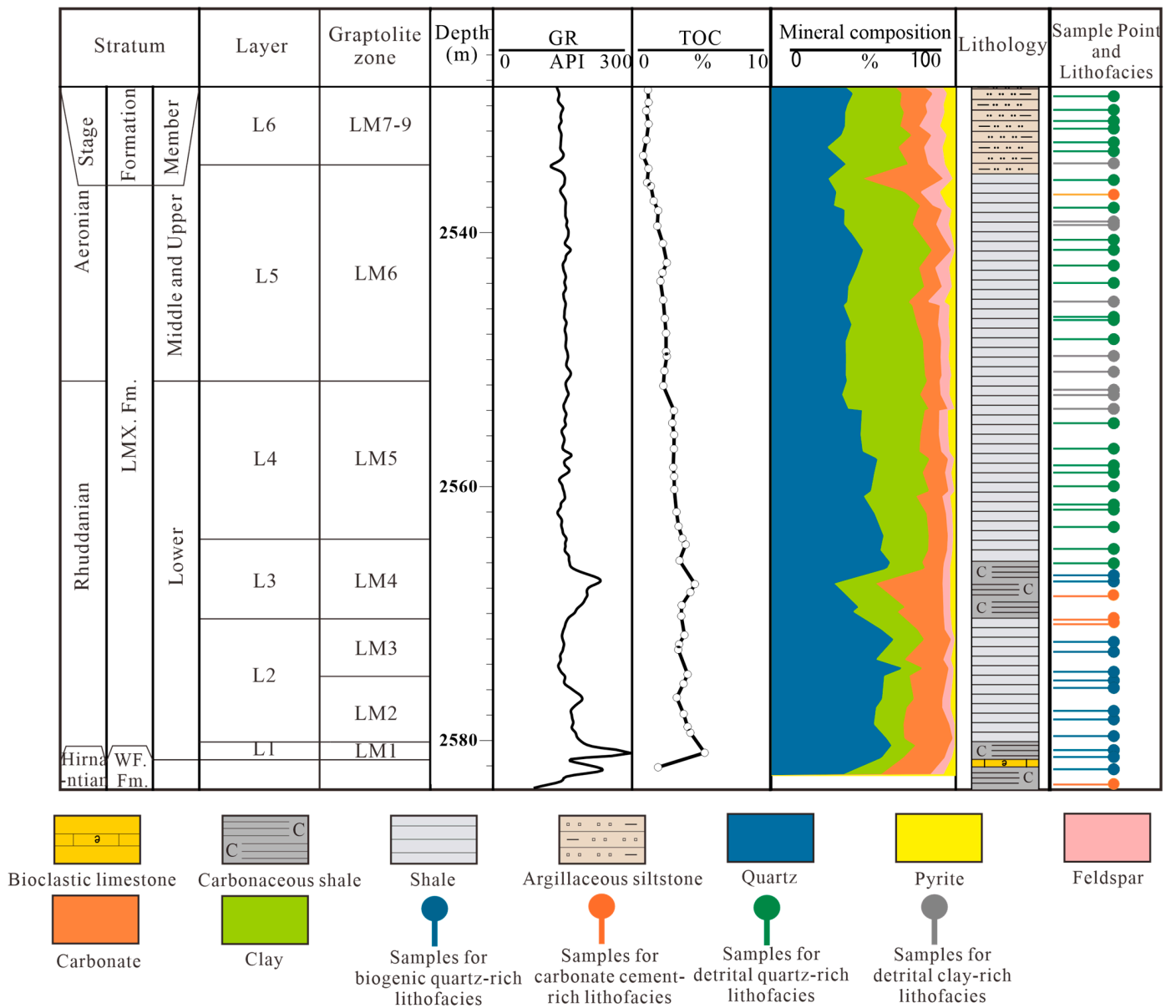


**Figure 2.** Stratigraphic framework, mineral composition, sample locations, and lithofacies classification for the Rhuddanian–Aeronian stage of Well N1. GR—natural gamma ray logging; Mem.—Member; LMX. Fm.—Longmaxi Formation; WF. Fm.—Wufeng Formation.

### 3. Samples and Methods

#### 3.1. Samples

The N1 Well, located on the southern flank of the Changning Anticline in the eastern part of the Changning block, provided 53 shale samples from the black shales of the Wufeng–Longmaxi Formation (Figure 2). Among these samples, 38 are siliceous shales, 10 are clay-rich shales, and 5 are calcareous shales. All 53 samples underwent X-ray diffraction analysis (XRD), thin-section examination, field emission–scanning electron microscopy (FE-SEM) analysis, scanning electron microscopy analysis (QEMSCAN), and total organic carbon testing (TOC). Additionally, 28 samples were tested for major and trace elements, followed by paleoenvironmental index calculations.

### 3.2. Methods

#### 3.2.1. Mineral Composition Measurements

The XRD analysis was carried out via a X-Pert-ProMPD X-ray diffractometer (Panalytical company, Amsterdam, Dutch). This process adhered to the analysis method for clay minerals and ordinary nonclay minerals in sedimentary rocks by X-ray diffraction ([5–7], SY/T5163-2018). The core samples were ground to pass through a 325-mesh sieve and tested at 20 °C, with a voltage of 40 kV and a current of 40 mA. The diffractometer was equipped with a Cu target (focus size: 12 mm × 0.4 mm) and a goniometer with a radius of 150 mm (Panalytical company, Amsterdam, Dutch).

To study the mineral size, content, and morphology, FE-SEM coupled with an EDAX energy-dispersive X-ray spectrometer was employed (EDAX Incorporated, New York, NY, USA). Forty-nine shale samples underwent mechanical polishing followed by ion polishing on a Gatan 600 DuoMill instrument (Gatan Incorporated, New York, NY, USA) at 4 kV and a low angle (7.5°) for 2 h. Further details on the milling and SEM observations are available in previous studies.

The QEMSCAN analysis was conducted by iCore Group Inc., Shenzhen, China, following the General Rules for Measurement of Length at the Micron Scale by SEM ([5–7], GB/T 16594-2008). The QEMSCAN test utilized a Quanta 650 SEM (Thermo Fisher Scientific, Prague, Czech Republic), operating at a voltage of 20 kV and a working distance of 13 mm, with backscatter mode imaging. All the experiments mentioned above regarding mineral characteristic analysis were carried out at the State Key Laboratory, Peking University, Beijing, China.

#### 3.2.2. TOC Measurements

We measured the TOC content in all the powdered samples (200–400 mesh) at Peking University via a LECO CS-400 carbon/sulfur analyzer ([5–7], LECO, New York, NY, USA). The process followed these steps: the samples were decarbonated by soaking them in 4 M hydrochloric acid (HCl) at 60 °C for at least 24 h, rinsing with distilled water to remove impurities and HCl, and then drying the samples. The precision of the TOC analysis was less than 0.10%, as verified by repeated standard sample tests. Additionally, the equivalent vitrinite reflectance was measured for 28 samples.

#### 3.2.3. Major and Trace Elements

We collected 28 relatively fresh and unweathered samples from Well A1 for major element concentration analysis via X-ray fluorescence (XRF, [14]). The samples were ground to 200 mesh and dried in an oven. Each sample, which was precisely weighed to 1.2 g, was mixed with 6 g of  $\text{Li}_2\text{B}_4\text{O}_7$  as a flux. This mixture was placed in a platinum crucible and melted at 1100 °C to form a homogeneous glass bead. The major elements analyzed included  $\text{SiO}_2$ ,  $\text{Al}_2\text{O}_3$ ,  $\text{Fe}_2\text{O}_3$ ,  $\text{CaO}$ ,  $\text{MgO}$ ,  $\text{K}_2\text{O}$ ,  $\text{Na}_2\text{O}$ ,  $\text{TiO}_2$ ,  $\text{P}_2\text{O}_5$ ,  $\text{MnO}$ ,  $\text{MnO}_2$ ,  $\text{BaO}$ , and  $\text{SO}_3$ . The analysis was performed via a ThermoFisher X-ray fluorescence spectrometer (New York, NY, USA). The precision of the major element analysis was less than 5%.

In this study, we analyzed the trace element concentrations of 28 samples via an inductively coupled plasma mass spectrometer ([14], ICP-MS, AMETEK, Berlin, Germany). Each 100 mg sample was dried at 105 °C and then dissolved in a mixture of 0.5 mL of  $\text{HClO}_4$ , 2.5 mL of  $\text{HF}$ , and 0.5 mL of  $\text{HNO}_3$ , followed by the addition of 1 mL of  $\text{HNO}_3$  and 3 mL of  $\text{H}_2\text{O}$ . The solution was then diluted and measured via ICP-MS. The analysis was monitored via standard samples OU-6 (shale), AMH-1 (andesite), and GBPG-1 (plagioclase), ensuring a precision of less than 0.5%. The testing was conducted at the School of Earth and Space Sciences, Peking University, China.

#### 3.2.4. Paleoenvironmental Index Calculation

The degree of elemental enrichment in sediments is often represented by the enrichment factor (EF). The enrichment factor (EF) is calculated via the formula provided by Munnecke [3]:

$$EF = (E/Al)_{\text{sample}} / (E/Al)_{\text{PAAS}} \quad (1)$$

where E represents the concentration of an element normalized to the post-Archean Australian shale (PAAS) standard [2,3]. An  $EF > 3$  indicates apparent enrichment,  $1 < EF < 3$  suggests moderate enrichment, and  $EF < 1$  denotes depletion, all in comparison to the PAAS standard [2,3].

In this study, 2 indicators, namely,  $Si_{xs}$  and  $Ba_{bio}$ , were employed to characterize the changes in paleoproductivity [56,57]. The  $Si_{xs}$  index is used to determine the content of biogenic silica, and the excess  $SiO_2$  content can be computed as follows:

$$Si_{xs} = Si_{\text{total}} - Al_{\text{total}} \times (Si/Al)_{\text{detrital}} \quad (2)$$

To elucidate paleoproductivity via Ba, it is essential to subtract the terrigenous components. The calculation for  $Ba_{bio}$  is as follows [56,57]:

$$Ba_{bio} = Ba_{\text{sample}} - Ti_{\text{sample}} \times (Ba/Ti)_{\text{PAAS}} \quad (3)$$

The chemical index of alteration (CIA) and the index of compositional variability (ICV) are commonly used to reflect the degree of source weathering and paleoclimate conditions. The CIA, proposed by Nesbitt and Young [58], is calculated via the following formula:

$$CIA = [(Al_2O_3)/(Al_2O_3 + CaO + Na_2O + K_2O)] \times 100 \quad (4)$$

CIA values less than 60 indicate a cold, dry, and weakly weathered paleoenvironment. CIA values between 60 and 80 suggest a warm, humid, and moderately weathered environment, whereas CIA values above 80 represent a hot, humid, and strongly weathered environment. The ICV is used to distinguish between recycled and first-cycle sediment sources. The calculation formula is as follows:

$$ICV = (Fe_2O_3 + K_2O + Na_2O + CaO^* + MgO + MnO + TiO_2) / Al_2O_3 \quad (5)$$

An ICV value less than 1 indicates compositionally mature sediments derived from recycled sources, whereas an ICV value greater than 1 represents compositionally immature sediments from first-cycle sources [50].

## 4. Results

### 4.1. Lithofacies Classification

Based on XRD and TOC data, samples with similar mineral compositions and TOC contents were selected for comparative analysis using hierarchical clustering methods. Furthermore, by integrating the analysis of QEMSCAN images, thin-section images, and FE-SEM images, four main lithofacies were identified during the Rhuddanian–Aeronian stage in the Changning area: detrital clay-rich lithofacies (CRDF), carbonate-rich lithofacies (CRF), biogenic quartz-rich lithofacies (BQRF), and detrital quartz-rich lithofacies (DQRF). These lithofacies exhibit significant differences in mineral composition, physical properties, and geochemical characteristics (Table 1, Figures 3–6).

The BQRF is mainly composed of siliceous shale, with quartz predominantly in the form of biogenic quartz. There are two types of biogenic quartz: quartz with biological structures and quartz without biological structures (Figures 5a–c and 6a–c). Quartz with biological structures retains the original biological framework, including radiolarians, sponge spicules, and fragments of thin-shelled mollusks, ranging from 2 to 600  $\mu\text{m}$  in size (Figures 5a–c and 6a,b). Quartz without biological structures is formed through the dissolution and reprecipitation of unstable biogenic silica in sediments, resulting in cryptocrystalline, microcrystalline, and microcrystalline aggregates with 6  $\mu\text{m}$  (Figure 6a–c). The quartz content often exceeds 60%, with the biogenic quartz content often above 25%. The average carbonate content is 14.2%, the average clay mineral content is 15.2%, and the average TOC content is 3.7% (Figures 3 and 4, Tables 1 and S1). DQRF also consists

mainly of siliceous shale, with a high content of amorphous detrital quartz (often above 25%, Figures 3, 4, 5d–f and 6d–f).

**Table 1.** Mineral composition, TOC, and distribution characteristics of four shale lithofacies developed during the Rhuddanian–Aeronian period.

Lithofacies	Primary Stratigraphic Distribution	Mineral Composition			Typical Mineral Characteristics	TOC Content (%)
		Clay Mineral (%)	Quartz (%)	Carbonate Mineral (%)		
Biogenic quartz-rich facies (BQRF)	L1–L3 Layers	56.3–70.0	56.3–70.0	9.7–25.4	Enriched in recrystallized quartz with biological structures and biogenic microcrystalline quartz.	3.2–4.2
Quartz-rich detrital facies (QRDF)	L4–L6 Layers	26.0–43.6	37.5–56.8	7.8–17.4	Enriched in anhedral, blocky detrital quartz with variable grain sizes.	0.9–3.5
Detrital clay-rich facies (CRDF)	L1–L3 Layers	40.1–48.5	32.0–43.3	6.9–14.8	High content of amorphous, oriented detrital clays that strongly obstruct intergranular pores.	1.0–2.5
Carbonate cement-rich facies (CCF)	L4–L6 Layers	19.1–25.1	31.0–46.8	7.2–43.7	Detrital calcite and early diagenetic carbonate cement widely developed.	0.7–3.2

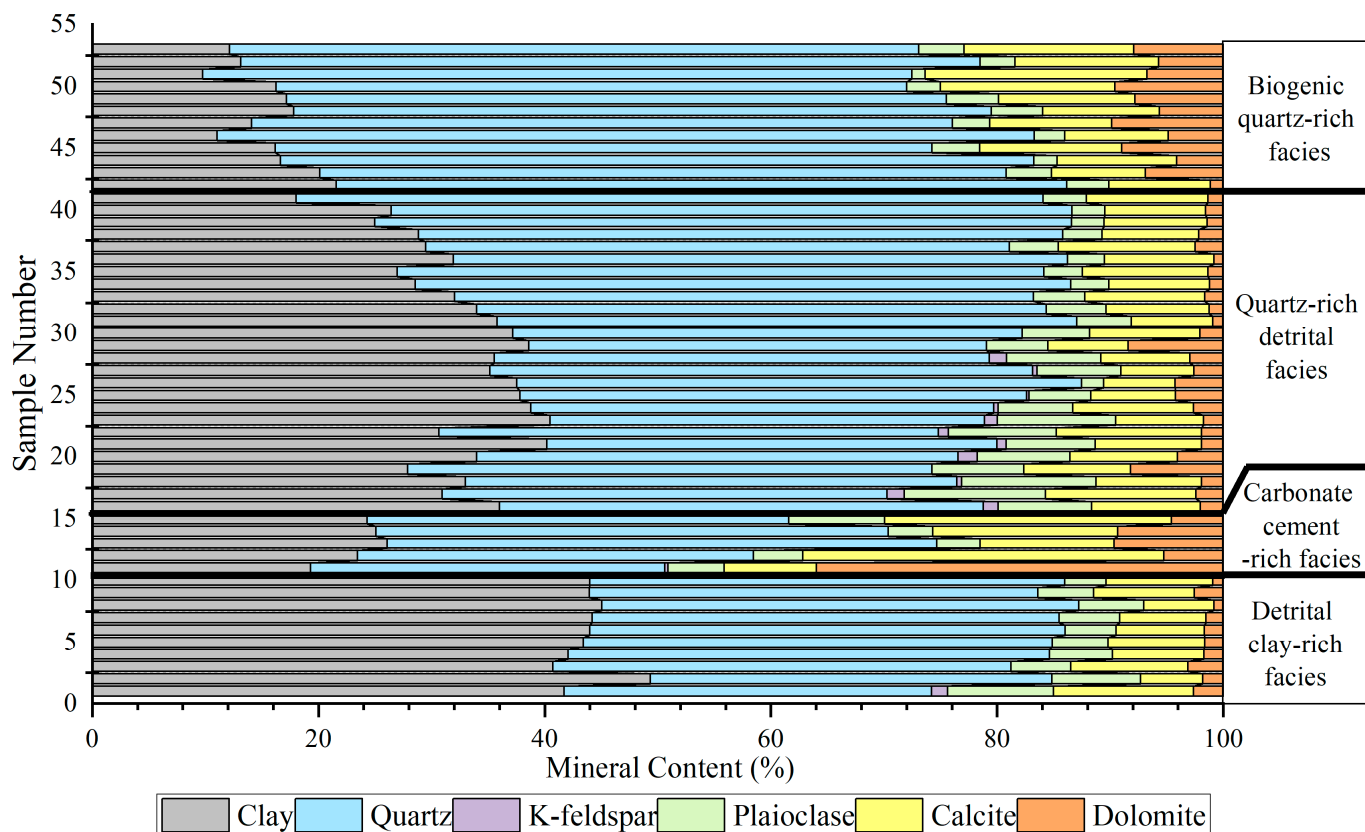


**Figure 3.** Mineral composition of four shale lithofacies developed in the Longmaxi Formation, N1 Well.

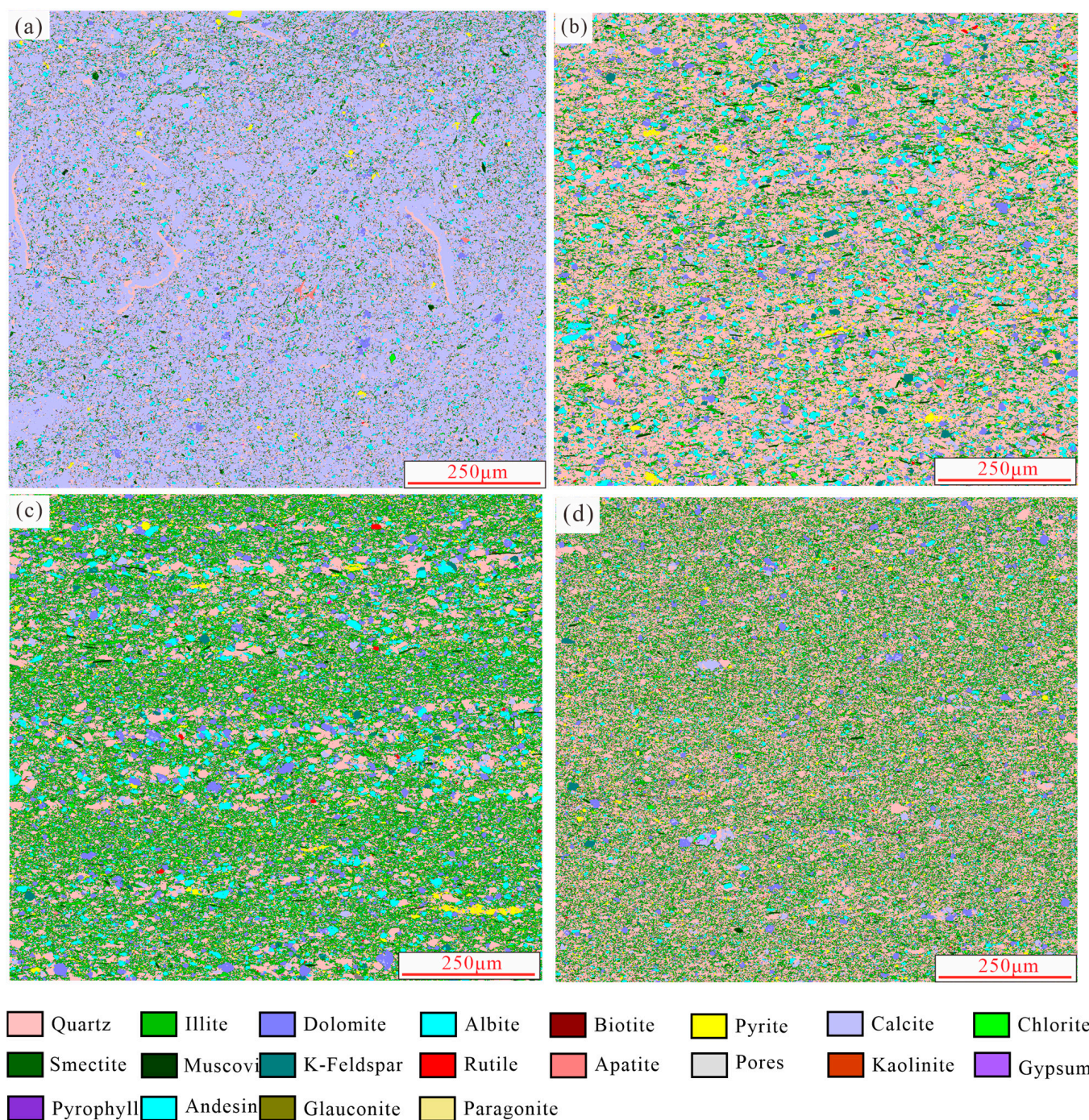


**Figure 4.** QEMSCAN image characteristics of four typical lithofacies developed in the Longmaxi Formation, N1 Well. (a) Representative sample image for carbonate rich lithofacies (CRF), 2566.9 m. (b) Representative sample image for biogenic quartz-rich lithofacies (BQRF), 2576.76 m. (c) Representative sample detrital clay-rich lithofacies (CRDF), 2532.82 m. (d) Representative sample image for quartz-rich detrital lithofacies (QRDF), 2531.72 m.

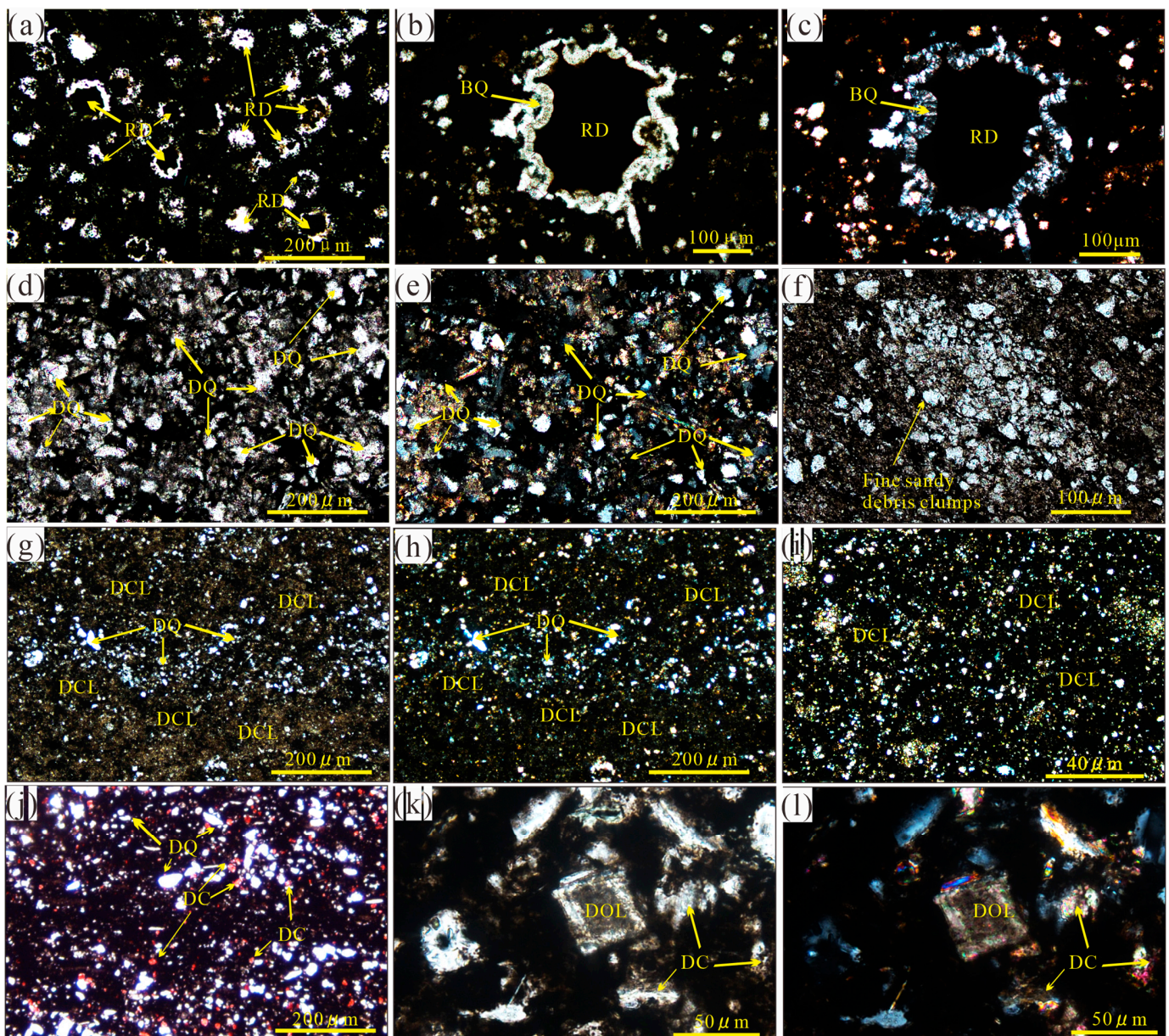


**Figure 5.** Thin-section images of representative shale samples from four lithofacies. (a) Abundant radiolarians with a diameter of approximately 50  $\mu\text{m}$  developed in the BQRF shale sample, under plane-polarized light, 2576.08 m; (b,c) radiolarian shells filled with biogenic quartz, BQRF representative sample, under plane-polarized light and cross-polarized light, 2551.04 m; (d,e) anhedral, irregularly shaped, and variably sized detrital quartz grains irregularly distributed, with detrital clay dispersed throughout, under plane-polarized light and cross-polarized light, DQRF representative sample, 2556.61 m; (f) detrital siltstone clasts are well-developed in the QRDF sample, under plane-polarized light, 2563.24 m; (g,h) amorphous detrital clay minerals are diffusely distributed, under plane-polarized light and cross-polarized light, CRDF representative sample, 2579.74 m; (i) some detrital clay minerals are distributed in clumps, CRDF representative sample, under cross-polarized light, 2545.09 m; (j) blocky detrital calcite distributed between minerals, stained with alizarin red, under plane-polarized light, CRF representative sample, 2580.71 m; (k,l) detrital calcite and non-ferroan rhombohedral dolomite, under plane-polarized light and cross-polarized light, CRF representative sample, 2580.71 m.

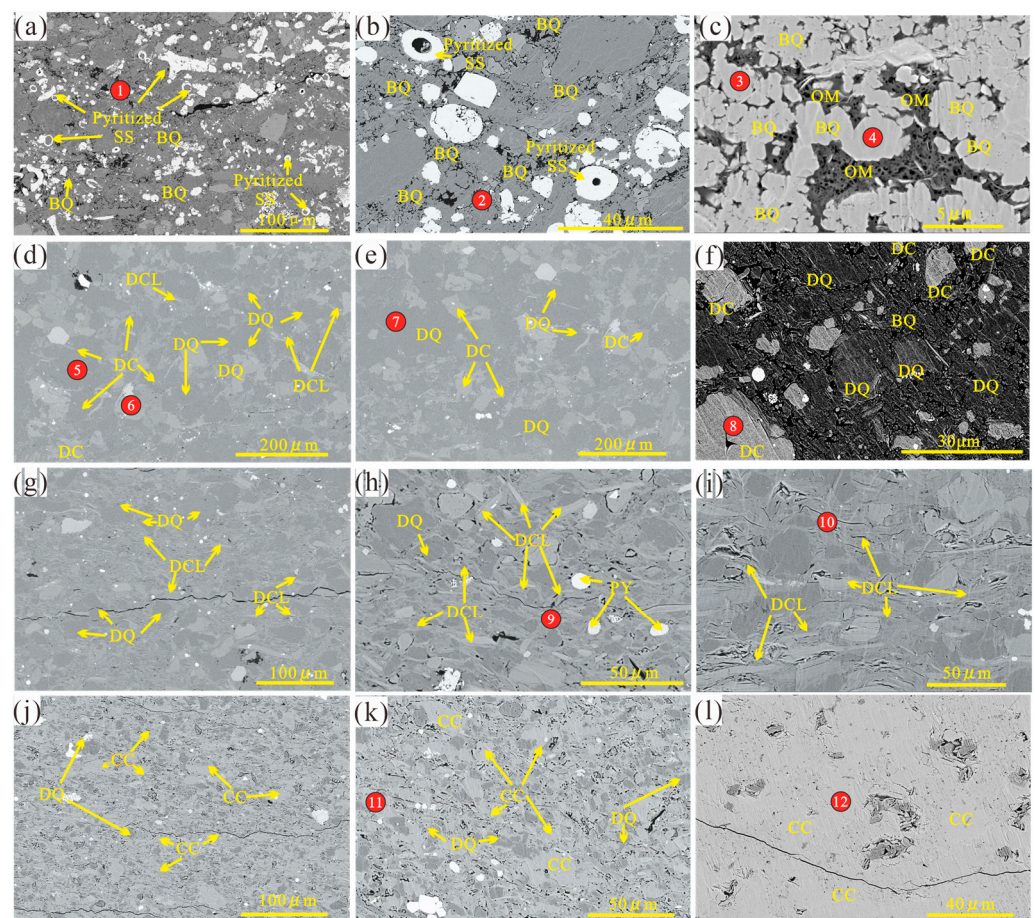


**Figure 6.** Scanning electron microscope images of representative samples of four lithofacies from the Rhuddanian–Aeronian period in Well N1. The marked points within the red circles in the scanning electron microscope (SEM) images represent the locations where energy-dispersive spectroscopy (EDS) data were collected. For detailed EDS data, please refer to Table S1 (a) Siliceous biogenic debris coexists with biogenic microcrystalline quartz, BQRF representative sample, 2576.08 m; (b) pyritized sponge spicules in association with biogenic microcrystalline quartz, representative sample, 2551.04 m; (c) intergranular pores in biogenic microcrystalline quartz filled with organic matter, representative sample, 2559.72 m; (d) anhedral detrital quartz is relatively well-developed in the QRDF representative sample, with occasional bent and striped detrital clay observed, 2563.24 m; (e) irregularly shaped detrital quartz and detrital calcite with concavo-convex grain contacts, QRDF representative sample, 2556.61 m; (f) a large amount of detrital quartz and detrital calcite exhibit irregular contact with low euhedral degree, QRDF representative sample, 2555.29 m; (g) detrital clay minerals are significantly affected by compaction, resulting in oriented alignment, CRDF representative sample, 2579.74 m; (h) densely packed detrital clay minerals filling intergranular pores, CRDF representative sample, 2551.75 m; (i) detrital clay deformed by compaction, bending and filling intergranular pores, CRDF representative sample, 2545.09 m; (j) syntaxial calcite cementation filling intergranular pores during syndiagenesis, CRF representative sample; (k) syndepositional calcite cement in a basal pattern filling the spaces between detrital quartz grains, CRF representative sample, 2580.71 m; (l) basal calcite cement filling intergranular pores with developed dissolution pores, CRF representative sample, 2578.08 m; (h) pyrite coexisting with early diagenetic non-ferroan dolomite, CRF representative sample, 2569.21 m. SS: sponge spicules; OM: organic matter; BQ: biogenic quartz; DC: detrital calcite; CC: calcite cement; DQ: detrital quartz; IPD: iron-poor dolomite; DCL: detrital clay; PY: pyrite.

The CRDF is characterized by poorly defined clay mineral boundaries and a high degree of detrital origin (Figures 5g–i and 6g–i). This facies consists mainly of gray-black or gray clayey shale, with clay mineral contents often exceeding 40% (Figures 3 and 4, Tables 1 and S1). The primary clay minerals identified are illite, illite–smectite mixed layers, and chlorite, with minor amounts of kaolinite. These clay minerals predominantly exhibit an amorphous morphology, with poorly developed crystal shapes (Figures 5g–i and 6g–i). They are significantly affected by compaction, often showing a tendency to align or tightly fill intergranular pores, and mostly consist of detrital calcite (Figures 5g–i and 6g–i). The average clay mineral content is 42.9%, the average quartz content is 39.1%, the average carbonate content is 10.2%, and the average TOC content is 2.1% (Figures 3 and 4, Tables 1 and S1). The CRF primarily comprises calcareous shale with a high content of detrital calcite and early diagenetic carbonate cement (Figures 5j–l and 6j–l). The detrital calcite typically appears as anhedral blocks with irregular edges. Early diagenetic carbonate cementation is mainly characterized by basal intercrystalline calcite and blocky to zoned dolomite (Figures 5k–l and 6j–l). The calcite content ranges from 8.1% to 24.3%, and the dolomite content ranges from 5.0% to 35.6%, with an average clay mineral content of 22.3%, an average quartz content of 38.2%, and an average TOC content of 4.3% (Figures 3 and 4, Tables 1 and S1).

## 4.2. Paleoenvironmental Proxies

### 4.2.1. Paleoredox Conditions

The redox conditions of mass water are critical factors influencing the preservation of organic matter [59]. In anoxic environments, organic matter can be well preserved and enriched [60]. Previous studies have shown that the presence and concentration of redox-sensitive elements such as U, Mo, and V in sediments vary with redox conditions [57]. Therefore, these elements are used to reconstruct the redox state of water during sedimentation. In this study, we used indicators such as V/Cr, Ni/Co, U/Th, V/Sc,  $Mo_{EF}$ , and  $U_{EF}$  to characterize the redox conditions of paleowater [60]. In Well N1 of the Longmaxi Formation, the U/Th ratio ranges from 0.20 to 2.63, the V/Cr ratio ranges from 1.3 to 6.0, the Ni/Co ratio ranges from 2.6 to 15.6, and the V/Sc ratio ranges from 8.3 to 49.2. The  $Mo_{EF}$  values range from 4.4 to 173.3, and the  $U_{EF}$  values range from 1.8 to 22.6 (Tables S2 and S3, Figure 7). These redox indicators generally tend to decrease from the bottom L1 Layer to the top L6 Layer, with slight increases in the V/Cr and Ni/Co ratios at the base of the L6 Layer (Figures 7 and 8). Specifically, in Layers L1–L3, the U/Th ratio ranges from 1.0 to 2.6, V/Cr from 6.0 to 2.2, Ni/Co from 0.59 to 0.70, and V/Sc from 17.0 to 49.2 (Figures 7 and 8).  $Mo_{EF}$  values range from 52.7 to 173.3, and  $U_{EF}$  from 6.2 to 22.6 (Figures 7 and 9a,b). In Layer L4, the U/Th ratio ranges from 0.4 to 1.0, V/Cr from 2.0 to 3.0, Ni/Co from 3.8 to 6.4, and V/Sc from 10.6 to 18.7 (Figures 7 and 8).  $Mo_{EF}$  values range from 11.2 to 57.3, and  $U_{EF}$  from 3.0 to 6.2 (Figures 7 and 9a,b). In Layers L5–L6, the U/Th ratio ranges from 0.2 to 0.5, V/Cr from 1.3 to 2.3, Ni/Co from 3.31 to 6.19, and V/Sc from 8.3 to 12.0 (Figures 7 and 8).  $Mo_{EF}$  values range from 4.4 to 17.1, and  $U_{EF}$  from 1.8 to 3.3 (Figures 7 and 9a,b).

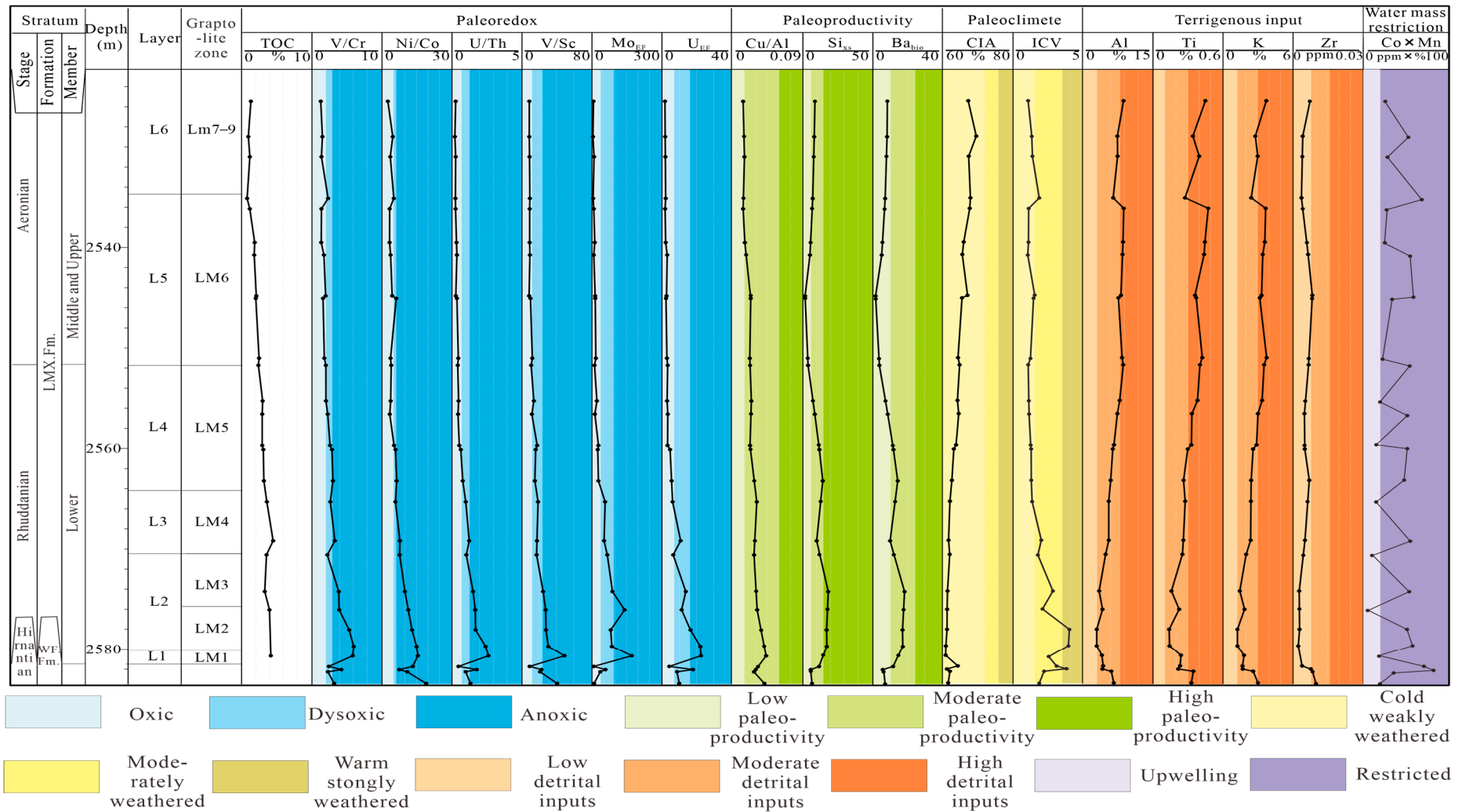


**Figure 7.** Vertical variation of geochemical characterization parameters in Well N1 for paleoenvironment during the Rhuddanian–Aeronian period. Mem.—Member; LMX Fm.—Longmaxi Formation; GYQ—Guanyinqiao Member; WF Fm.—Wufeng Formation; LX Fm.—Linxiang Formation.

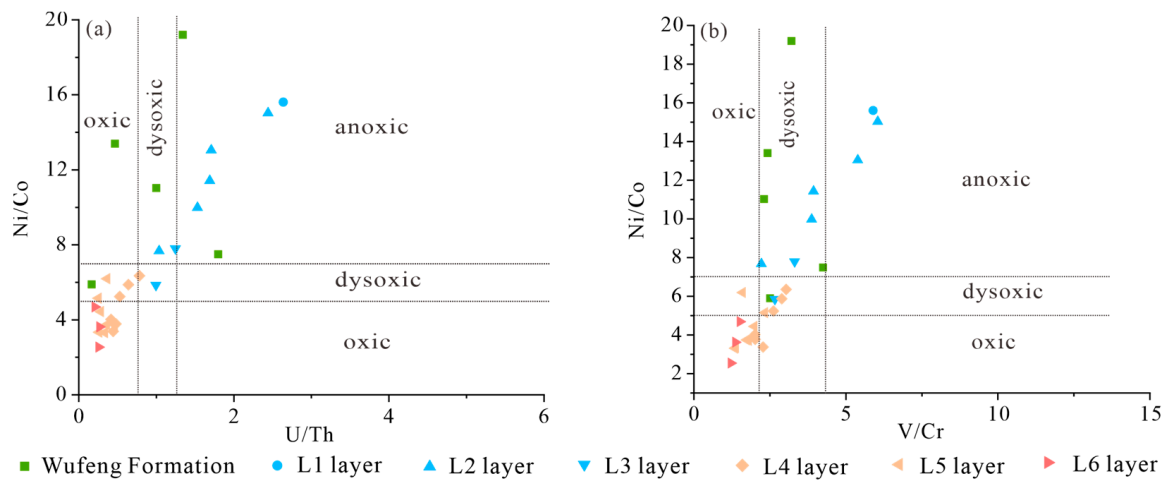


**Figure 8.** Correlation plots of paleoredox indicators for seven layers during the Rhuddanian–Aeronian period in Well N1: (a) Ni/Co vs. U/Th; (b) Ni/Co vs. V/Cr.

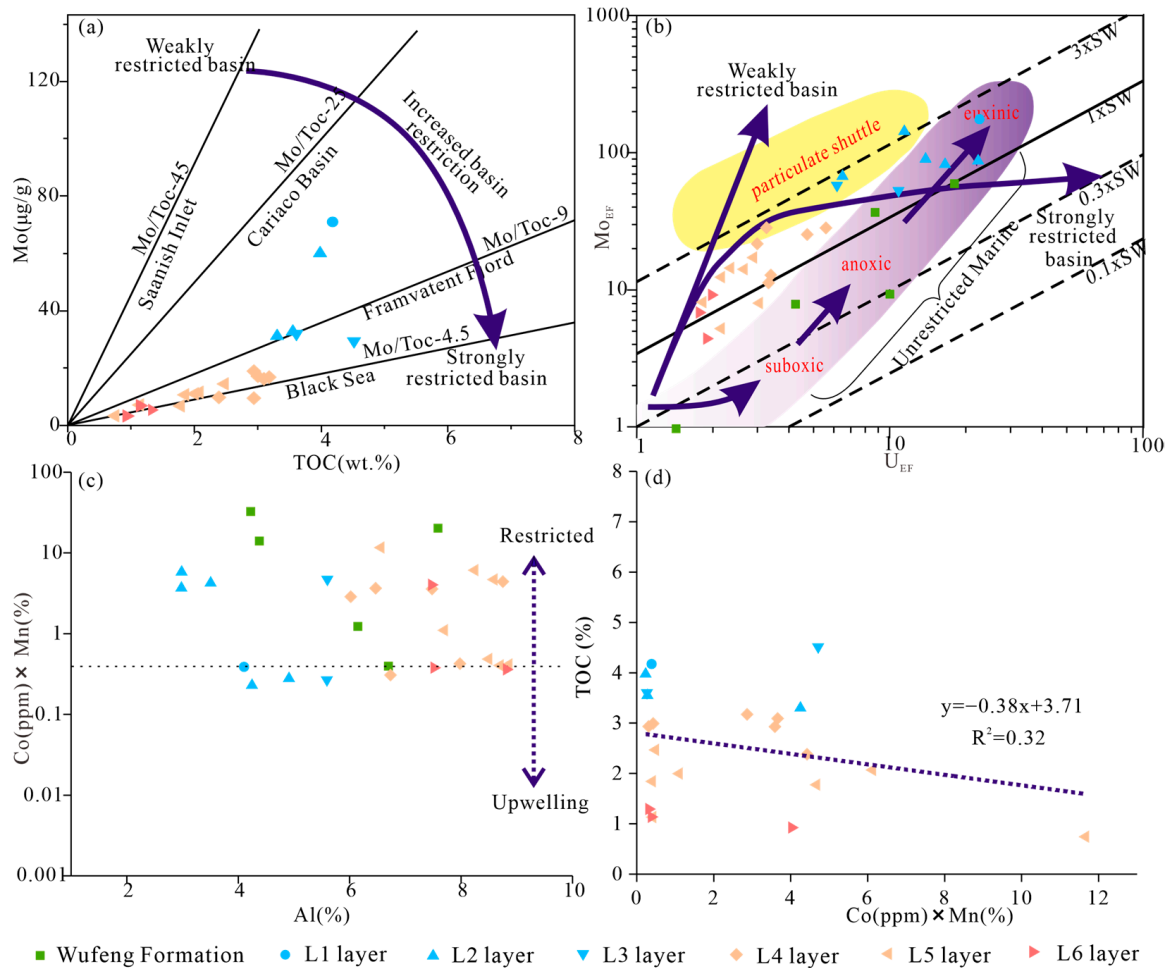


**Figure 9.** Plots illustrating water mass restriction levels across seven layers during the Rhuddanian–Aeronian transition in Well N1: (a) Mo–TOC relationships compared to modern anoxic stilled-basin environments; (b)  $Mo_{EF}$  vs.  $U_{EF}$ ; (c)  $Co \times Mn$  vs. Al; (d) TOC vs.  $Co \times Mn$ .

#### 4.2.2. Degree of Seawater Restriction

The  $Mo_{EF}$ – $U_{EF}$  diagram is often used to characterize the degree of water mass restriction [1,61,62]. Typically, higher Mo/U ratios in sediments indicate stronger water mass

restriction, whereas lower Mo/U ratios suggest weaker restriction and an environment more similar to seawater [1,61,62]. In Well N1, the  $Mo_{EF}-U_{EF}$  ratios from the L1 to L6 Layers mostly fall between 1 and  $3 \times SW$ , indicating a gradual increase in water mass restriction and oxidation levels (Tables S2 and S3, Figure 9a,b).

Similarly, the Mo–TOC diagram is frequently used to assess water mass restrictions. Under stronger restrictions, the Mo/TOC ratio tends to be lower, whereas in less restricted environments, where the molybdenum (Mo) supply is more ample, the Mo/TOC ratio is usually greater (Figure 9a,b, [1,61,62]). Consistent with the  $Mo_{EF}-U_{EF}$  diagram results, the average Mo/TOC ratios for Layers L1 to L6 are 17.0, 11.3, 7.7, 5.0, 5.4, and 4.8, respectively, showing a decreasing trend from L1 to L6 (Figure 9a). The depositional environment from Layers L4 to L6 corresponds to a sedimentary model similar to that of the Black Sea (Figure 9a, [61,62]).

In this study, the Co\*Mn ratio was used to indicate the influence of upwelling on the deposition of the Longmaxi Formation in Well N1 [63]. Scholars generally believe that the stronger the influence of upwelling on sediments is the greater the extent to which Co\*Mn values are less than 0.4 [63]. In Well N1, the Co\*Mn values range from 0.23 to 14.04 in the lower parts of Layers L1 to L2, whereas in Layer L3, the Co\*Mn values exceed 2.5, ranging from 0.3 to 4.7 (Figure 9c). The Co\*Mn values in Layers L4 to L6 gradually increase and are all greater than 0.4 (Figure 9c). According to Figure 9d, there is a significant negative correlation between the TOC and Co\*Mn values in the Longmaxi Formation samples from Well N1, indicating a close relationship between upwelling and organic matter enrichment in the Longmaxi Formation shales (Figure 9d).

#### 4.2.3. Paleoproductivity

Paleoproductivity is closely related to nutrient levels in water, as a relatively high nutrient supply leads to increased biological activity [56,57]. This, in turn, enhances the ability of organisms to fix carbon through photosynthesis, thereby increasing productivity. Factors affecting paleoproductivity include upwelling, hydrothermal activity, and volcanic activity [56,57]. Geochemical indicators often used to indicate changes in paleoproductivity include stable carbon and nitrogen isotopes, molecular biomarkers, TOC content, and the abundance of trace elements such as Ba, P, Cu, Ni, and Zn [56,57].

In this study, paleoproductivity was estimated using the Cu/Al ratio, excess silica ( $Si_{XS}$ ), and biogenic barium ( $Ba_{bio}$ ) content ([56,57], Tables S2 and S3, Figure 7). From the L1 to L5 Layers in Well N1, Cu/Al,  $Si_{XS}$ , and  $Ba_{bio}$  values generally decrease, with a slight increase from mid-L5 to the top of L6 (Figure 7). Specifically, the  $Si_{XS}$  ratio and  $Ba_{bio}$  values range as follows: 10.0–21.6 and 0.02–0.09 in L1–L3; 3.8–14.4 and 0.04–0.14 in L4; 1.6–7.1 and 0.01–0.07 in L5; and 7.0–8.2 and 0.03–0.07 in L6 (Figure 7).

#### 4.2.4. Terrigenous Inputs

Terrigenous detrital input plays a role in injecting nutrients, diluting organic matter, and controlling burial rates. Therefore, the composition and amount of detrital input directly affect organic matter enrichment in black shales [59]. Elements such as Al, Ti, K, and Zr, owing to their high stability and minimal influence from postdepositional weathering and diagenetic processes, are commonly used to reflect the input of terrigenous materials [1,50]. K and Al originate from clay minerals in aluminosilicates, Ti is present as ilmenite and  $TiO_2$  in sediments, and Zr often comes from stable heavy minerals [1,50].

In this study, variations in Al, Ti, K, and Zr contents were used to track changes in terrigenous detrital input in the Longmaxi Formation of Well N1 (Figures 7 and 10). From Layers L1 to L2, the input remained low, gradually increasing from L1 to L4 (Figures 7 and 10). In Layer L5, the element contents stabilized, with a slight decrease at the bottom of L6 (Tables S2 and S3, Figures 7 and 10). Specifically, the average contents of Al, Ti, Zr, and K were 4.3%, 0.21%, 32.6 ppm, and 1.8% in Layers L1 to L3; 7.4%, 0.34%, 59.9 ppm, and 3.0% in L4; 7.7%, 0.40%, 62.2 ppm, and 3.4% in L5; and 7.5%, 1.6%, 2.3 ppm, and 2.9% in L6 (Figures 7 and 10).

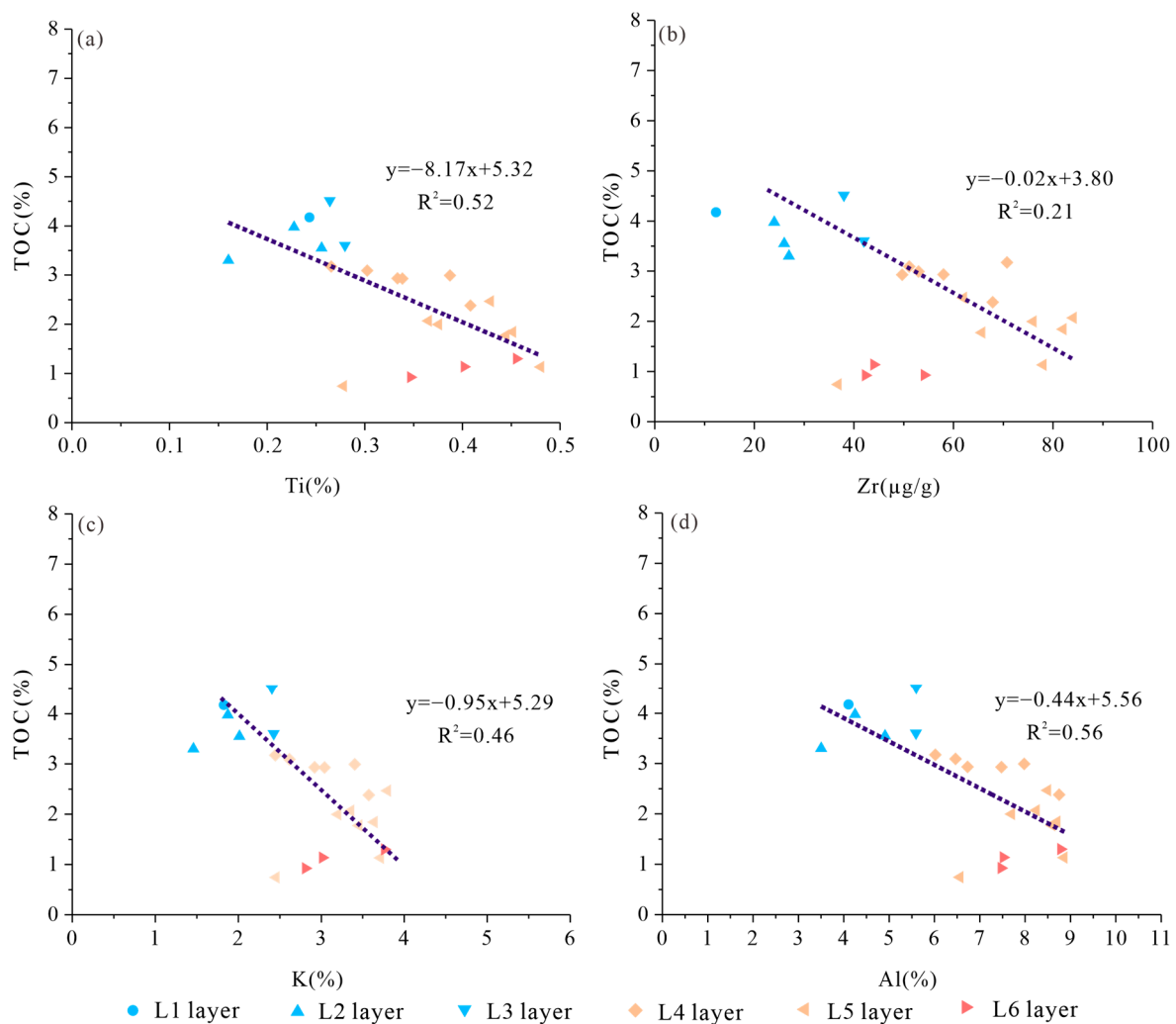


**Figure 10.** Correlation analysis of TOC with terrigenous detrital input indicators: (a) TOC vs. Ti; (b) TOC vs. Zr; (c) TOC vs. K; (d) TOC vs. Al.

Additionally, the contents of Al, Ti, Zr, and K are negatively correlated with TOC, with Al and Ti exhibiting stronger negative correlations than K and Zr do (Figure 10). This indicates that the terrigenous detrital supply mainly comes from clay minerals and Ti-bearing detrital minerals (Figures 7 and 10).

#### 4.2.5. Paleoclimate

In this study, the CIA, ICV, and Rb/Sr ratio were used to characterize the paleoclimate changes during the deposition of the Longmaxi Formation in Well N1 ([3,50,58,62], Figures 5 and 9, Tables S2 and S3). The average CIA value for the Longmaxi Formation in Well N1 is 72.1 (Figure 11a), and the average ICV value is 1.7, indicating moderate chemical weathering (Figure 11b). From Layers L1 to L5, the CIA gradually increased, whereas the ICV continuously decreased, suggesting that the sediments were primarily first-cycle deposits with increasing chemical weathering (Figures 7 and 11). In Layer L6, the CIA slightly decreases, and the ICV slightly increases, indicating a minor shift in weathering intensity (Figures 7 and 11).

Specifically, in Layers L1 to L3, the CIA values range from 69.8 to 74.2, and the ICV values range from 1.4 to 4.1 (Figures 7 and 11). In Layer L4, the CIA values range from 72.8 to 74.0, and the ICV values range from 1.1 to 1.3 (Tables S2 and S3, Figures 7 and 11). In Layer L5, the CIA values range from 66.9 to 74.6, and the ICV values range from 1.1 to 1.9

(Figures 7 and 11). In Layer L6, the CIA values range from 68.0 to 68.9, and the ICV values range from 1.3 to 1.4 (Figures 7 and 11) [53].

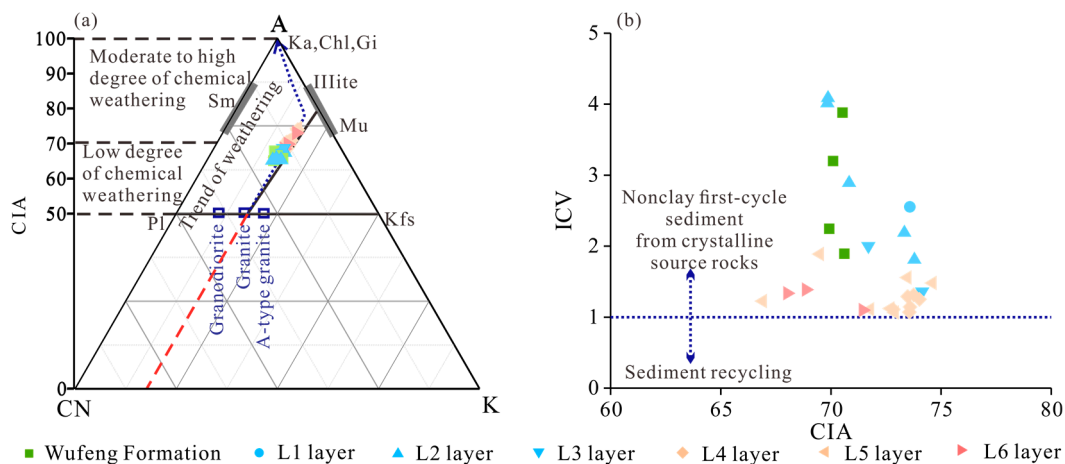


**Figure 11.** Weathering intensity diagrams: (a) A-CN-K weathering intensity plot; (b) ICV-CIA weathering degree plot. The CIA and ICV identification diagrams were modified in [50,58]. Ka: kaolinite; Chl: chlorite; Gi: gibbsite; Sm: smectite; Mu: muscovite; Pl: plagioclase (Pl); Kfs: k-feldspar; CIA: chemical index of alteration; ICV: index of compositional variability; A: content of  $\text{Al}_2\text{O}_3$ ; CN: content of  $\text{CaO} + \text{Na}_2\text{O}$ ; K: content of  $\text{K}_2\text{O}$ .

## 5. Discussion

### 5.1. Changes in the Paleoenvironment during the Rhuddanian–Aeronian Stages

#### 5.1.1. Early Rhuddanian: Anoxia and High Paleoproductivity Driven by Rapid Sea Level Rise

Following the Hirnantian period, global temperatures rose rapidly in the Early Rhuddanian, causing the glaciers on the Gondwana continent to melt and triggering rapid marine transgression [5,52,53]. During this time, black shales began to be deposited in deep-water shelf areas [53]. The rapid transgression led to rapid increases in the concentrations of V, Ni, and U, as the redox conditions of the bottom water shifted from low oxygen to strongly anoxic. V/Cr ratios above 4.25, Ni/Co ratios above 7, and U/Th ratios above 1.25 indicate an anoxic environment during the Rhuddanian (Figures 7 and 8). The rapid increase in water column anoxia, the sudden appearance of large quantities of radiolarians and sponge spicules, and the abrupt fining of grain size in the siliceous shale indicate a rapid sea-level rise (Figures 2, 5a–c, 6a,b and 7). The rapid rise in sea level increased the connectivity between the Middle Yangtze Sea and the Qinling Ocean, reducing the degree of basin restriction [8,9,51,52]. This resulted in a rapid increase in the Mo/U ratios and Co\*Mn values compared with those of the Hirnantian stage (Figure 9). The end of the Hirnantian glaciation caused a temperature gradient between the bottom and surface waters, leading to stratification [42]. The rapid consumption of dissolved oxygen in surface waters significantly increased the anoxic conditions in the bottom waters, while upwelling currents developed ([64,65], Figure 9c,d). High values of  $\text{Si}_{\text{xs}}$ ,  $\text{Ba}_{\text{bio}}$ , and  $\text{Cu}/\text{Al}$  suggest high paleoproductivity levels during the Rhuddanian, likely due to the postglacial bloom of plankton and the upwelling of nutrient-rich deep waters ([56,57], Figures 7 and 9c,d). The low terrigenous input during the Rhuddanian may have resulted from weaker chemical weathering due to the lower global temperatures during the Hirnantian glaciation [3,61,62]. This period is characterized by rapid sea level rise, anoxic water conditions, high paleoproductivity, moderate upwelling intensity, rising paleotemperatures, and low terrigenous input (Figure 7). These combined environmental factors facilitated the rapid deposition and preservation of biogenic remains and siliceous skeletons under anoxic–euxinic conditions, leading to the widespread formation of BQRF [44–48].

### 5.1.2. Late Rhuddanian to Early Aeronian: Increased Terrigenous Input and Oxidation during Sea-Level Regression

During the Late Rhuddanian period (L4 Layer deposition), the Kwangsian Orogeny progressed, causing the Upper Yangtze Plate to slowly uplift and resulting in a significant drop in sea level [5,52,53]. This led to the mixing of oxygenated surface waters with anoxic bottom waters, greatly increasing the oxygen content of the water column. The values of V/Cr, Ni/Co, U/Th, V/Sc,  $M_{\text{OEF}}$ , and  $U_{\text{EF}}$  rapidly decreased, indicating a transition in redox conditions from anoxic to dysoxic (Figures 7 and 9). Concurrently, the decrease in the Mo/U ratio suggested an increase in water mass restriction, likely due to further uplift of the Central Guizhou uplift, Central Sichuan uplift, and Xuefeng uplift influenced by the Kwangsian orogeny ([7,64–66], Figures 7 and 9). As the intensity of upwelling and volcanic activity weakened, the amount of nutrients from the seabed significantly decreased ([4], Figure 7). This led to a slowdown in the growth rate of lower organisms and a decline in primary productivity, as reflected in the rapid decreases in the  $Si_{\text{xs}}$ ,  $Ba_{\text{bio}}$ , and Cu/Al values (Figure 7). The rapid increase in CIA, Al, Ti, Zr, and K contents indicates an increase in paleotemperature and enhanced chemical weathering, resulting in a significant increase in terrigenous detrital input, reflecting the onset of an interglacial period with global warming and increased chemical weathering ([8], Figures 7, 10 and 11).

During the L5 Layer deposition (the Early Aeronian stage), the intensity of the Kwangsian orogeny significantly weakened, leading to a slower uplift of paleouplifts and regional tectonic elevation [67,68]. The depositional environment remained highly restricted and oxidized, with slight increases in  $Si_{\text{xs}}$ ,  $Ba_{\text{bio}}$ , and Cu/Al values during the middle-L5 Layer deposition, indicating a minor increase in paleoproductivity (Figure 7). The stable contents of Al, Ti, Zr, and K suggest consistent terrigenous input, whereas increasing CIA and decreasing ICV values indicate a continued increase in paleotemperature and enhanced chemical weathering (Figures 7, 10 and 11). Thus, the Early Aeronian period was characterized by high sedimentation rates, increased oxygen levels in bottom waters, and substantial terrigenous input [5,40,52]. The continuous increase in terrigenous input led to the widespread development of the DQRF and CRDF. The dilution effect of terrigenous detritus and poor preservation conditions resulted in a lower organic matter content in these shales.

### 5.1.3. Middle Aeronian: Paleoenvironmental Changes Driven by Interglacial Sea Level Fluctuations

During the Middle Aeronian period (L6 Layer deposition), the V/Cr and Ni/Co ratios slightly increased, and the shale grain size generally became finer (Figures 2, 5, 6 and 8). Combined with the decrease in  $\delta^{18}\text{O}$  and the increase in  $\delta^{13}\text{C}$ , these changes indicate a slight and relatively stable rise in sea level, accompanied by a minor decrease in oxygen levels in the water column, briefly creating dysoxic conditions ([6,53,65,66], Figures 7 and 8b). The degree of water mass restriction remained strong (Figure 9). At this time, the values of  $Si_{\text{xs}}$ ,  $Ba_{\text{bio}}$ , and Cu/Al continued to fluctuate, indicating a slight overall increase in paleoproductivity during the middle to Late Aeronian period (Figure 7). Moreover, the terrigenous detrital input indicators, i.e., Al, Ti, Zr, and K, slightly decreased, suggesting a gradual reduction in terrigenous detrital input (Figures 7 and 10). The slight decrease in the CIA indicates localized cooling during this period (Figures 7 and 11). The overall environment was characterized by frequent and unstable climate disturbances typical of an interglacial period, with a slight rise in sea level, a modest increase in paleoproductivity, and a decrease in terrigenous detrital input (Figures 7 and 10). During this time, the predominant shale lithofacies were CRF and CRDF [45,48].

## 5.2. Impacts of Paleoenvironmental Transformations on Lithofacies

### 5.2.1. BQRF Formation in Anoxic, High-Paleoproductivity Deep-Water Shelves

In the shale samples from the L1–L6 Layers, quartz can be morphologically classified into three types: microcrystalline quartz, recrystallized quartz within siliceous biogenic

shells, and detrital quartz (Figures 5a–f and 6a–f). The BQRF shale samples are characterized by the extensive development of microcrystalline quartz, which is preliminarily attributed to biogenic activity. This inference is supported by three main lines of evidence: (1) The TOC content positively correlates with the excess Si content in the L1–L6 Layers, indicating a significant contribution of biogenic silica to the total silica content (Figure 12a). Similar findings have been reported in other studies [11]. Notably, the correlation between  $Si_{xs}$  and TOC is significantly stronger in BQRF compared to other lithofacies, confirming that biogenic silica is the predominant source of excess Si in BQRF (Figure 12a). In contrast, the CRDF and CRF show no clear positive correlation between TOC and  $Si_{xs}$ , suggesting that in these lithofacies, TOC may have other non-biogenic sources, such as organic matter from terrigenous detritus (Figure 12a). (2) The majority of BQRF samples in this study exhibit a negative correlation, further suggesting that much of the silica is of biogenic origin ([10–15], Figure 12b). Conversely, DQRF, CRF, and a small number of CRDF samples align with the detrital trend, indicating a minor contribution of silica from the detrital sediment fraction ([10–15], Figure 12b). (3) In the excess Si-enriched intervals of the L1–L3 Layers, a large amount of siliceous bioclastic material is often observed, frequently associated with microcrystalline quartz and organic matter (Figure 6a–c). In Well N1, the  $Si_{xs}$  values in the samples of L1–L3 Layers often exceed 15%, while in the L4 Layer, six values mostly exceed 10%, confirming the enrichment of excess Si in the L1–L4 Layers (Figure 7). Siliceous bioclasts, including radiolarians, sponge spicules, and fragments of thin-shelled mollusks, are commonly observed in the L1–L4 Layers (Figures 5a–c and 6a,b). These siliceous bioclasts are often associated with equigranular microcrystalline quartz, indirectly supporting the biogenic origin of equigranular microcrystalline quartz, as shown in Figure 10a,b. Additionally, in the BQRF of the L1–L3 Layers, either interparticle pores or bitumen fillings are commonly found between individual quartz grains within the aggregates of euhedral quartz (Figure 6c). In contrast, interparticle pores and organic pores are much less abundant between the clay matrix-dispersed microquartz (Figure 6d–f). However, in the L4–L6 Layers, the six values are often below 5%, indicating that excess Si is not well-developed in these layers (Figure 7). Scanning electron microscope images of the L4–L6 Layers show a lack of microcrystalline quartz and siliceous bioclasts that are commonly observed in the L1–L4 Layers (Figure 6d–f). The quartz in these layers predominantly appears as irregularly shaped, uneven-edged detrital quartz, as shown in Figures 5d–f and 6d–f. The presence of detrital quartz in the L4–L6 Layers indirectly suggests that the microcrystalline quartz observed in the L1–L4 Layers may be related to the presence of excess Si.

Based on the aforementioned evidence, it can be concluded that the majority of microcrystalline quartz in the BQRF was formed through the dissolution and reprecipitation of unstable biogenic silica within sediments. The microcrystalline quartz frequently replaces cavities within radiolarians and sponge spicules, filling approximately 30%–40% of the cavity volume. This observation suggests that the quartz formation occurred prior to significant mechanical compaction and is closely related to siliceous skeletal organisms [12–15,69]. During burial, the high-solubility amorphous quartz (opal-A/opal-CT) from radiolarians and sponge spicules gradually transforms into low-solubility, stable cryptocrystalline, microcrystalline, and coarse-grained quartz under the influence of elevated temperature and pressure [69]. Thus, a key characteristic of BQRF is the high content of biogenic silica, often exceeding 25%.

The high paleoproductivity of bottom waters during the Early Rhuddanian was the primary reason for the abundant biogenic quartz, which was evident in two aspects: (1) The high quartz content sections coincided with high paleoproductivity sections (Figures 2, 7 and 13), indicating that synsedimentary volcanic activity and upwelling provided rich nutrients, significantly enhancing surface water productivity [8]. Therefore, high paleoproductivity provided a rich material basis for the formation of biogenic quartz. The skeletal fragments of siliceous zooplankton, such as radiolarians, sponge spicules, and diatoms, are intrabasinal components that originate from the surface water column under conditions of sufficient nutrient supply [20,42].

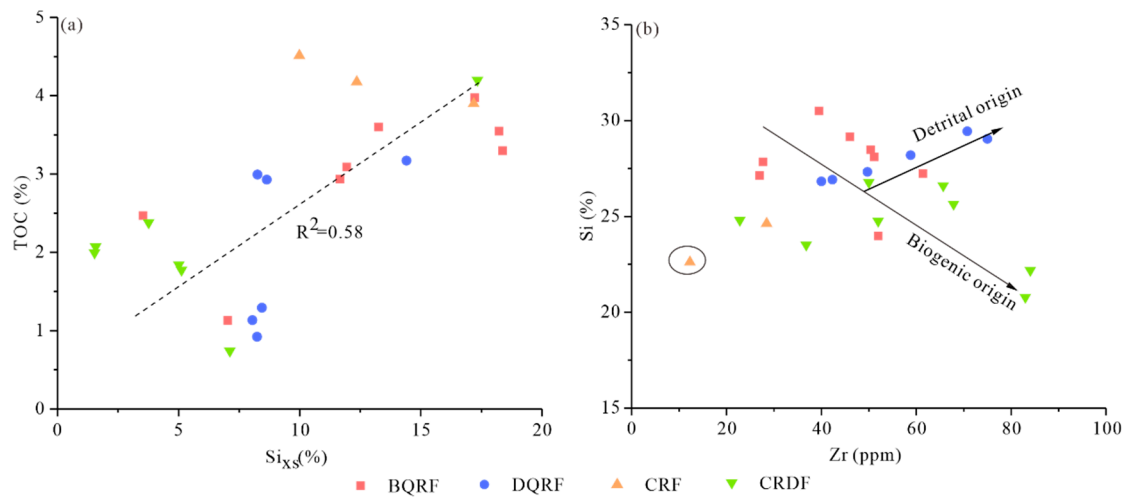


**Figure 12.** Source discrimination diagrams of Si element in four shale lithofacies (modified from [10–15]). (a) TOC vs. Si<sub>XS</sub>; (b) Si vs. Zr.

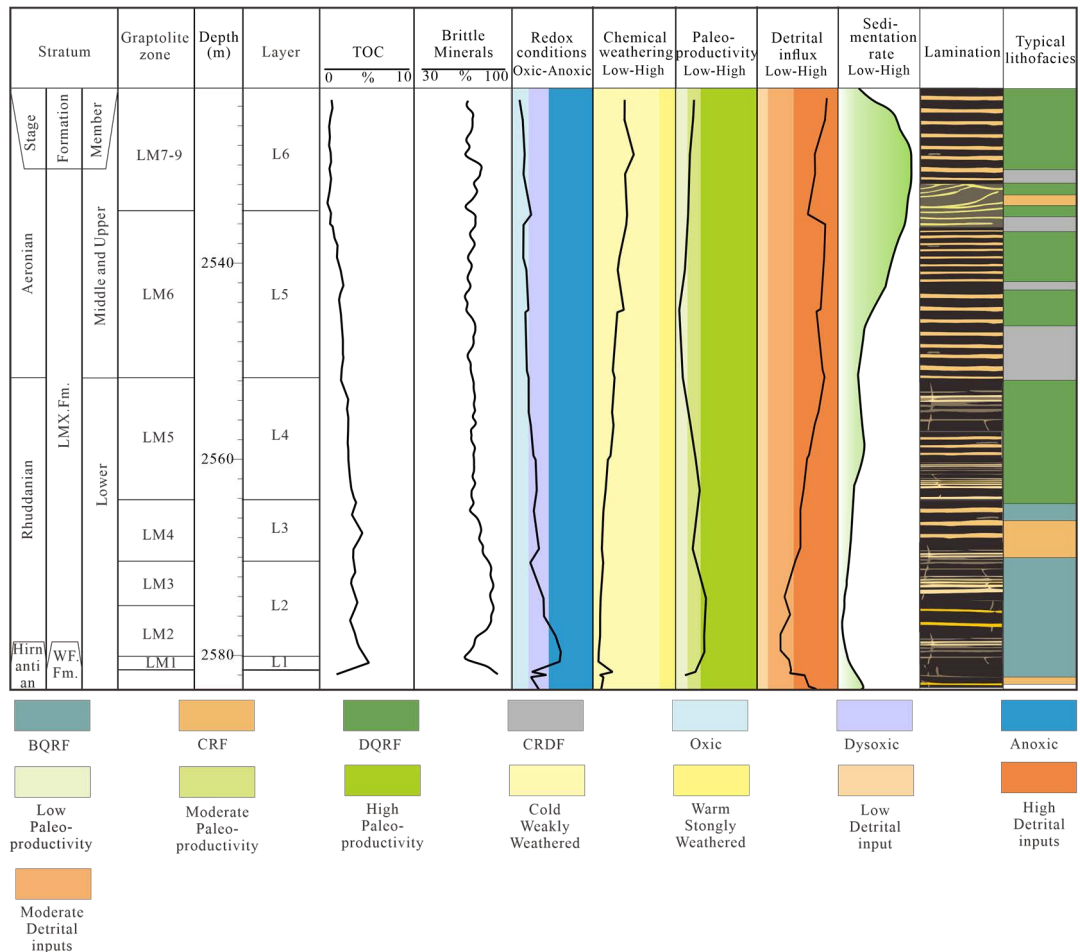


**Figure 13.** Schematic diagram of the relationship between paleogeographic environments and lithofacies types during the Rhuddanian–Aeronian period in Well N1. GR—natural gamma ray logging; Mem.—Member; LMX. Fm.—Longmaxi Formation; WF. Fm.—Wufeng Formation; CRF: carbonate rich lithofacies; BQRF: biogenic quartz-rich lithofacies; CRDF: detrital clay-rich lithofacies; QRDF: quartz-rich detrital lithofacies.

The second characteristic of BQRF is its high organic matter content (Figures 7 and 13), which is due to high paleoproductivity and favorable preservation in anoxic conditions during the Rhuddanian. High productivity means rapid growth and reproduction of siliceous skeletal organisms in surface waters, with their remains settling to the seafloor as organic matter is deposited [10,13,15]. Rapid marine transgression and high oxygen consumption in bottom waters created anoxic to anaerobic conditions, slowing organic matter degradation and enhancing preservation [10,13,15]. Therefore, BQRF sediments mainly consist of biogenic quartz, with minor detrital clay minerals and carbonates. They form under high paleoproductivity, anoxic to anaerobic conditions, and low-energy environments in deep-water shelves, resulting in finely laminated BQRF ([53], Figures 13 and 14).

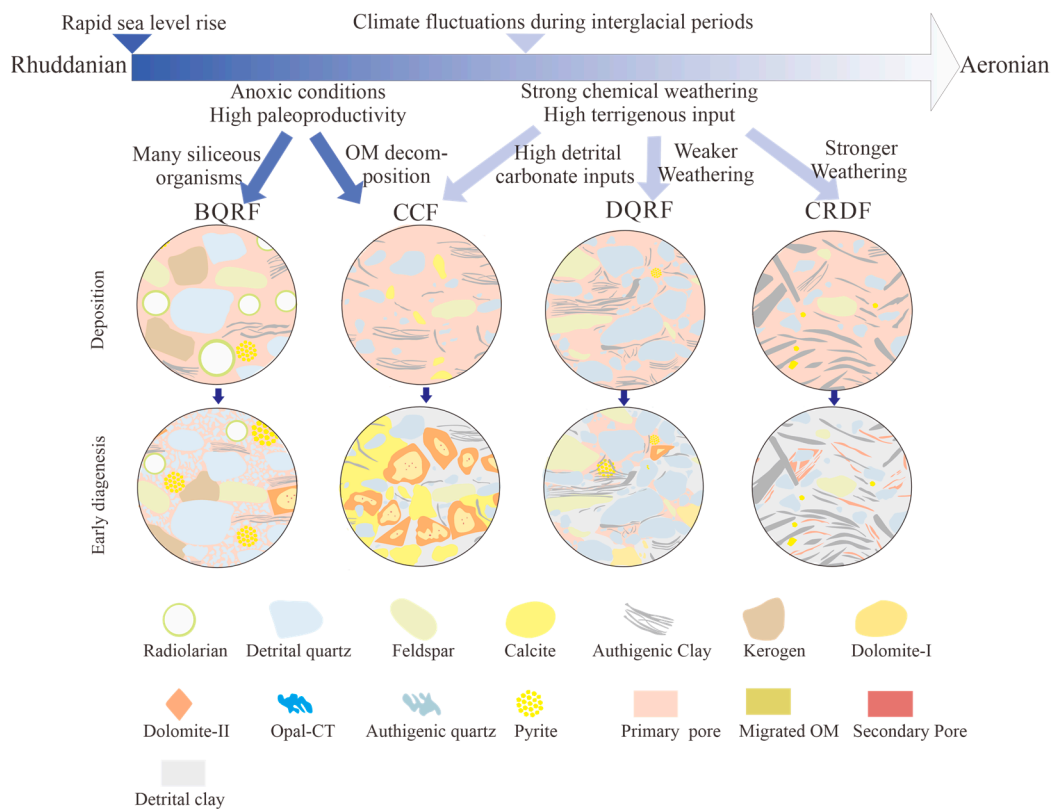


**Figure 14.** Model diagram of the influence of paleoenvironmental changes on the formation processes of four lithofacies during the Rhuddanian–Aeronian period. CRF: carbonate-rich lithofacies; BQRF: biogenic quartz-rich lithofacies; CRDF: detrital clay-rich lithofacies; QRDF: quartz-rich detrital lithofacies; OM: organic matter.

### 5.2.2. Effects of Interglacial Sea Level and Climate Fluctuations on CRDF and DQRF

CRDF and DQRF often form in environments characterized by strong chemical weathering, warm and humid conditions, and significant terrigenous detrital input (Figures 7 and 13). These lithofacies were developed predominantly in the Late Rhuddanian and Aeronian periods (Figure 13). Compared with the Early Rhuddanian, the shale during this time was primarily composed of detrital quartz, as evidenced by two factors: (1) Detrital quartz grains are larger (Figure 6d–f, typically 50–800  $\mu\text{m}$ ), with irregular and poorly defined boundaries, unlike microcrystalline quartz and biogenic quartz with biological structures ([69], Figure 6a–c); (2) the correlation between the TOC content and detrital quartz content in the L4–L6 Layers was weaker than that in the L1–L3 Layers, indicating that biogenic quartz was no longer the main quartz type in the Late Rhuddanian to Aeronian period (Figures 2, 7 and 13). The clay minerals in this period are also mainly detrital, characterized by the following features: (1) Detrital clay minerals are predominantly anhedral, making it difficult to identify their types on the basis of morphology, and they are

tightly packed due to strong compaction ([7,65], Figures 5g–i and 6g–i). (2) The variation trends of the clay mineral content in the Rhuddanian to Aeronian shales are consistent with the changes in Al and K, suggesting that terrigenous detrital input is the primary source of clay minerals, with minor contributions from diagenetic clays formed during burial (Figures 7 and 13). During the Late Rhuddanian to Early Aeronian, the paleotemperature gradually increased, and the climate was warm and humid.

The surrounding uplifts of the Sichuan basin were more strongly affected by chemical weathering, which primarily supplied detrital clay [50]. The rapid increase in K and Al contents in the sediments supports this view (Figures 7 and 11). In the Mid-Aeronian, fluctuations in the interglacial climate caused a slight decrease in paleotemperature and rapid weakening of the chemical weathering intensity [6,7,65]. Consequently, the primary type of terrigenous detritus shifted from detrital clay to detrital quartz, leading to the widespread development of the DQRF (Figures 11 and 13). Furthermore, the formation of the CRDF and DQRF was influenced by the water flow velocity and the rate of terrigenous detrital input (Figures 7 and 13, [53,54]). Both the CRDF and DQRF exhibit graded horizontal bedding, indicating that silt and clay particles from terrigenous sources settled as flocculated particles, which were affected by bottom currents, causing them to break apart and reform into sand laminae [53,54]. When the water flow velocity exceeded 25 cm/s, silt laminae composed mainly of detrital quartz formed, whereas lower flow velocities resulted in clay laminae [53,54]. Thus, the widespread development of the CRDF and DQRF is attributed to strong weathering under warm and humid conditions and substantial terrigenous input (Figures 13 and 14). Climate fluctuations during the interglacial periods led to variations in weathering intensity, causing the alternating development of the CRDF and DQRF [44–46].

### 5.2.3. Controls on CRF Development: Paleoproductivity, Anoxic Conditions, and High Terrigenous Input

CRF were predominantly developed in the Early Rhuddanian (L1–L3 Layers) and mid-Aeronian (L5–L6 Layers) period. The carbonate minerals in the CRF mainly include detrital calcite, syndimentary calcite, and poorly ferroan dolomite (Figures 5j–l and 6j–i, [70–72]). Detrital calcite, commonly found in the Middle Aeronian beds, typically fills intergranular pores as amorphous aggregates with minimal recrystallization and alteration ([70–72]). Shale samples with high terrigenous detrital input often contain significant amounts of detrital calcite, as evidenced by two factors: (1) Amorphous calcite aggregates coexist with detrital quartz, forming silt laminae ([70–72], Figure 5j). (2) This phenomenon is more pronounced in samples with high Al contents, indicating that strong weathering of the parent rock during terrigenous sediment deposition contributed detrital materials, including clay minerals, feldspar, quartz, and minor calcite, which were transported to the deep-water shelf for deposition ([73], Figures 7 and 10). The high Al content suggests that the shale contains numerous terrigenous detrital minerals, including calcite and transported silicate minerals (Figures 7 and 10). Syndimentary basal cement calcite predominantly developed in the Early Rhuddanian time, appearing as intergranular fillings and filling cavities in radiolarians, ostracods, and sponge spicules (Figure 6j–l, [70–72]). The formation of syndimentary calcite is controlled mainly by high paleoproductivity and anoxic conditions. The high paleoproductivity in the Rhuddanian led to the absorption of  $\text{Ca}^{2+}$  and  $\text{CO}_3^{2-}$  by planktonic organisms to form skeletons or shells, which, after settling and dissolving, were deposited on the seabed and buried [70–74]. These carbonate-rich remains, upon the death of the organisms, became a significant source of calcite, explaining the frequent filling of biogenic cavities with calcite [70–74]. Moreover, high-productivity plankton reduce the pH of seawater through photosynthesis, promoting calcite formation. Rapid marine transgression deepened the water, creating anoxic conditions that slowed organic matter decomposition and preserved  $\text{Ca}^{2+}$ - and  $\text{CO}_3^{2-}$ -rich sediments, forming calcite [70–72]. Poorly ferroan dolomite, which is also enriched in Early Rhuddanian shales, is characterized by rhombohedral crystals and zonal structures [74]. Scholars often believe that this dolomite precipitated directly from pore fluids or was associated with sulfate reduction pro-

cesses [12,75,76]. This study suggests that the formation of iron-poor dolomite in the CRF of the Early Rhuddanian was driven primarily by sulfate reduction processes, as iron-poor dolomite and pyrite consistently cooccur within the same laminae (Figure 5k–l). Although this type of dolomite often forms in the sulfate reduction zone during early diagenesis, low sulfate concentrations in pore waters further promote microbial reduction, creating a suitable reducing environment for the precipitation of iron-poor dolomite [12,75,77]. The high paleoproductivity and anoxic conditions of the Early Rhuddanian provided crucial material support for its formation. During periods of high paleoproductivity, intense biological activity rapidly depletes dissolved oxygen and nutrients (such as phosphates and nitrates) in seawater ([78], Figure 13). The regeneration of these nutrients aids in the formation of iron-poor dolomite. For example, the decomposition of biological remains may release magnesium and other ions, facilitating dolomite formation. Sulfate-reducing bacteria play a key role in this process [12,76,78]. In high-productivity environments, abundant organic matter supplies these bacteria with ample nutrients, increasing their activity. Additionally, anoxic conditions resulting from rapid marine transgression promote active sulfate reduction by these bacteria. This not only lowers the pH but also reduces the contents of elements such as iron (Fe) and manganese (Mn) in the sediments, releasing cations such as magnesium, which combine with carbonate ions to form iron-poor dolomite [77]. In contrast, iron-rich dolomite is less prevalent in the Early Rhuddanian CRF, typically appearing as zoned or rhombohedral crystals. Scholars believe that this type of dolomite may be associated with methanogenic bacteria reduction and organic matter decarboxylation processes [12,75–78].

Overall, the development of CRF in the Early Rhuddanian was controlled by high paleoproductivity and anoxic conditions, with carbonate types consisting mainly of syndimentary calcite and early diagenetic iron-poor dolomite. In the Mid-Aeronian, CRF development was influenced by rapid sedimentation rates, substantial terrigenous input, intense physical and chemical weathering, and oxidizing conditions. Periodic changes in terrigenous input during interglacial periods led to the alternating development of clay-rich layers, detrital quartz-rich layers, and carbonate-rich layers (Figure 14).

### 5.3. Implications for Shale Gas Exploration

The organic-rich shales of the Rhuddanian–Aeronian period were formed through the combined influence of paleo-tectonics, paleoclimate, and paleoenvironmental factors, directly or indirectly impacted by various geological events [1–5]. The content of brittle minerals, TOC, and the composition of shale lithofacies serve as integrated records of paleogeographic evolution and are critical for shale gas reservoir exploration and evaluation. By comparing the paleoenvironmental characteristics, lithofacies types, TOC, and brittle mineral content during the Rhuddanian–Aeronian period, two types of favorable organic-rich shale reservoirs were identified. The first type (Type I) is the BQRF found in the L1–L3 Layers, and the second type (Type II) is the DQRF located in the L4 Layer (Figure 13).

As a Type I-favorable reservoir, the BQRF developed in the early L1–L3 Layers are characterized by high organic matter content and strong reservoir brittleness, with brittle mineral content ranging from 73% to 92% and TOC from 3.8% to 6.5% (Table 1, Figure 13). During the deposition of the L1–L3 Layers, the paleoenvironment was marked by low bottom current velocities, minimal clastic supply, slow deposition rates, anoxic conditions, and high paleoproductivity, all of which contributed to the enrichment of organic matter (Figures 7 and 13). The high content of biogenic quartz in these layers further supports their classification as favorable reservoirs. Many scholars have noted that biogenic microcrystalline quartz aggregates positively influence the development of pore networks (Figure 7, [10–15]). These aggregates not only provide space for the formation of organic pores but also act as a rigid framework that preserves the pore network by forming intergranular pores [12,13]. Consequently, both intergranular and organic pores are well preserved. Additionally, the early formed biogenic microcrystalline quartz aggregates exhibit high compressive strength, which likely results in the formation of slip seams between quartz aggregates and organic matter under external stress [10–15]. This process can

create effective flow channels during hydraulic fracturing, enhancing both the high yield and stable production of shale gas [15]. Therefore, the high TOC and abundant biogenic microcrystalline quartz in the BQRF of the L1–L3 Layers are crucial for the formation of Type I-favorable reservoirs. The authigenic microcrystalline quartz filling the intergranular pores supports the pore network, while the rich organic matter generates numerous organic pores and methane during gas generation.

The Type II-favorable reservoirs are primarily developed within the DQRF of the L4 Layer, which formed during the Late Rhuddanian period. These reservoirs have relatively high organic matter and brittle mineral content, though levels are lower than those found in the BQRF of the L1–L3 Layers. The brittle mineral content in Type II reservoirs ranges from 64% to 75%, with TOC levels between 2.5% and 3.6% (Table 1, Figures 7 and 13). During the deposition of the L4 Layer, sea levels began to decline, and the paleoenvironment gradually shifted from anoxic to suboxic conditions (Figure 13). Although paleoproductivity decreased and the input of terrigenous clastics increased, the paleoenvironment during the L4 deposition still maintained relatively high paleoproductivity and suboxic conditions compared to the Aeronian period, favoring organic matter preservation (Figures 7 and 13) [10–15]. This period also coincided with the onset of glaciation and the Guangxi orogeny, leading to a rise in paleotemperature and increased terrigenous clastic input, which contributed to the widespread development of DQRF and an increase in detrital quartz content. Compared to biogenic microcrystalline quartz, detrital quartz contributes less to shale reservoir quality, a difference closely related to their distribution, grain morphology, and mechanical properties [10]. Biogenic microcrystalline quartz in BQRF typically occurs as equiaxed microcrystals with uniform particle shape and size (Figure 6a–c) [15]. This uniformity reduces the “cushioning effect” between grains of varying sizes, meaning that under high stress conditions, stress distribution between grains is more even, reducing the likelihood of localized stress concentrations, grain slippage, or deformation [10–15]. Additionally, some scholars have found that biogenic microcrystalline quartz arranges more densely and stably during compaction, effectively suppressing the rolling effect between rounded grains [10–15]. In contrast, the more irregular shape and varying grain size of detrital quartz make it more prone to rolling under stress, potentially reducing the overall stability of the shale reservoir (Figure 6d–f, [10–15]). Nonetheless, compared to the CRF and the CRDF, DQRF still makes a significant contribution to shale reservoir properties. Detrital quartz, with its high hardness, brittleness, compressive strength, and chemical stability, continues to provide a substantial amount of primary porosity to the shale reservoir [13].

Notably, other scholars have also identified multiple transgressions during the Rhuddanian–Aeronian period [33,53,54], and it is widely accepted that there is a strong correlation between sea level rise and the extensive development of organic-rich shales. The rapid transgressions during the Early Rhuddanian period are generally recognized as having played a decisive role in the large-scale enrichment of organic matter [33,40]. In this study, we found that during the Mid-Aeronian period (L6 deposition), the V/Cr, Ni/Co, and U/Th ratios increased, indicating a slight upward fluctuation in sea level, possibly related to interglacial climate disturbances (Figures 7 and 13). Similar phenomena have been observed by other scholars in the Luzhou area of the Sichuan Basin [33]. However, the trend of TOC content during the Mid-Aeronian period shows little correlation with the paleo-oceanic redox conditions, weathering intensity, paleoproductivity, or terrigenous clastic input, suggesting that the small-scale transgressive events caused by interglacial climate disturbances had a limited impact on the large-scale enrichment of organic matter (Figures 7 and 13).

As a result, the Type I-favorable shale gas reservoirs developed in the L1 Layer have already been successfully exploited on a large scale, and the BQRF in the L2–L3 Layers holds promise for continuing high shale gas production of the Sichuan basin. The Type II-favorable reservoir in the L4 Layer can serve as a potential exploration target as a backup for the Type I shale gas reservoirs.

## 6. Conclusions

- (1) Four lithofacies developed in the Changning area of southern Sichuan Province during the Rhuddanian to Aeronian period: CRF, BQRF, CRDF, and DQRF. CRF is commonly found in the Early Rhuddanian and Middle Aeronian beds, characterized by a carbonate mineral content exceeding 30%, and mainly comprises detrital calcite, syngedimentary basal cement calcite, and zoned iron-poor dolomite. The CRF and DQRF developed primarily in the Late Rhuddanian to the Middle Aeronian strata. The CRF typically contains more than 40% detrital clay, whereas the DQRF often contains more than 20% detrital quartz. BQRF is frequently observed in the Early Rhuddanian, distinguished by high biogenic quartz content, high TOC, and well-developed horizontal lamination, with biogenic quartz content generally exceeding 25%.
- (2) During the Rhuddanian to Aeronian period, the paleoenvironment underwent significant changes, transitioning from an open water environment with active upwelling currents, low bottom water oxygen levels, high paleoproductivity, low terrigenous input, and a cold, arid climate to a highly restricted water environment with high oxygen levels, reduced paleoproductivity, increased terrigenous input, and a warm, humid climate. The Mid-Aeronian age experienced a brief dysoxic environment due to interglacial sea-level and climate changes, accompanied by a slight increase in paleoproductivity, reduced terrigenous input, and localized cooling. These paleoenvironmental changes were influenced mainly by the Kwangsi orogeny, interglacial climate fluctuations, and sea-level changes.
- (3) Paleoenvironmental changes directly controlled the shifts in lithofacies types from the Rhuddanian to the Aeronian age. BQRF typically formed in the Early Rhuddanian under anoxic water conditions, high paleoproductivity, and low terrigenous input in a calm water environment. The development of the CRDF and DQRF was influenced mainly by intense weathering and substantial terrigenous input in a warm and humid environment from the Late Rhuddanian to the Middle Aeronian age. Interglacial climate fluctuations led to changes in weathering intensity and water flow rates, causing alternating occurrences of the CRDF and DQRF. The Early Rhuddanian CRF was primarily controlled by high paleoproductivity and anoxic conditions, with carbonate types comprising mainly syngedimentary calcite and early diagenetic iron-poor dolomite. The extensive development of CRF in the Mid-Aeronian age was also the result of rapid sedimentation rates, high terrigenous input, intense physical and chemical weathering, and oxidizing conditions.
- (4) Two favorable shale gas reservoirs from the Rhuddanian–Aeronian period were identified: Type I (BQRF) in the L1–L3 Layers and Type II (DQRF) in the L4 Layer. Type I is distinguished by high TOC and strong brittleness, driven by biogenic quartz content, which enhances gas production and stability. Although Type II has lower TOC and brittle minerals, its detrital quartz content still makes a significant contribution to reservoir quality. The study emphasizes the crucial influence of Early Rhuddanian transgressions on organic matter enrichment, while noting the limited impact of Mid-Aeronian transgressive events. Therefore, the BQRF in the L1–L3 Layers supports ongoing shale gas production, with the DQRF in the L4 Layer offers potential as a future exploration target.

**Supplementary Materials:** The following supporting information can be downloaded at: <https://www.mdpi.com/article/10.3390/min14090949/s1>. Table S1: EDS data of key minerals in SEM images of typical samples from the Wufeng–Longmaxi Formation, Well N1; Table S2: Mineralogical composition characteristics of four lithofacies developed in the Wufeng–Longmaxi Formation in the N1 Well; Table S3: Major oxide contents, minor element contents, and paleoenvironment proxies of the Wufeng–Longmaxi Formation samples from the N1 Well.

**Funding:** This work is not supported by any funding projects.

**Data Availability Statement:** Data is contained within the article or Supplementary Materials.

**Conflicts of Interest:** Author Hangyi Zhu was employed by the company Research institute of Petroleum exploration and development. The author declare that the research was conducted in the absence of any commercial or financial relationships that could be construed as a potential conflict of interest.

## References

1. Tribovillard, N.; Algeo, T.J.; Lyons, T.; Riboulleau, A. Trace metals as paleoredox and paleoproductivity proxies: An update. *Chem. Geol.* **2006**, *232*, 12–32. [[CrossRef](#)]
2. Delabroye, A.; Vecoli, M. The end-Ordovician glaciation and the Hirnantian Stage: A global review and questions about Late Ordovician event stratigraphy. *Earth-Sci. Rev.* **2010**, *98*, 269–282. [[CrossRef](#)]
3. Munnecke, A.; Calner, M.; Harper, D.A.T.; Servais, T. Ordovician and Silurian sea—Water chemistry, sea level, and climate: A synopsis. *Palaeogeogr. Palaeoclimatol. Palaeoecol.* **2010**, *296*, 329–340. [[CrossRef](#)]
4. Qiu, Z.; Li, Y.; Xiong, W.; Fan, T.; Zhao, Q.; Zhang, Q.; Wang, Y.; Liu, W.; Liang, F.; Zhang, J.; et al. Revisiting paleoenvironmental changes on the Upper Yangtze Block during the Ordovician-Silurian transition: New insights from elemental geochemistry. *Sediment. Geol.* **2023**, *450*, 106377. [[CrossRef](#)]
5. Xi, Z.; Tang, S.; Lash, G.G.; Ye, Y.; Lin, D.; Zhang, B. Grain assemblages and diagenesis in Ordovician-Silurian transition shale deposits of the Upper Yangtze Platform, South China. *J. Asian Earth Sci.* **2022**, *230*, 105188. [[CrossRef](#)]
6. Feng, Y.; Xiao, X.; Gao, P.; Wang, E.; Hu, D.; Liu, R.; Li, G.; Lu, C. Restoration of sedimentary environment and geochemical features of deep marine Longmaxi shale and its significance for shale gas: A case study of the Dingshan area in the Sichuan basin, South China. *Mar. Petrol. Geol.* **2023**, *151*, 106186. [[CrossRef](#)]
7. Li, S.; Zhou, Z.; Nie, H.; Liu, M.; Meng, F.; Shen, B.; Zhang, X.; Wei, S.; Xi, Z.; Zhang, S. Organic matter accumulation mechanisms in the Wufeng-Longmaxi shales in western Hubei Province, China and paleogeographic implications for the uplift of the Hunan-Hubei Submarine high. *Int. J. Coal Geol.* **2023**, *270*, 104223. [[CrossRef](#)]
8. Xu, L.; Huang, S.; Wang, Y.; Zhou, X.; Liu, Z.; Wen, Y.; Zhang, Y.; Sun, M. Palaeoenvironment evolution and organic matter enrichment mechanisms of the Wufeng-Longmaxi shales of Yuanán block in western Hubei, middle Yangtze: Implications for shale gas accumulation potential. *Mar. Petrol. Geol.* **2023**, *152*, 106242. [[CrossRef](#)]
9. Xiong, M.; Chen, L.; Tan, X.; Chen, X.; Zheng, J.; Yang, Y.; Jing, C.; Wang, G. Effects of the astronomical orbital cycle on organic matter accumulation during the Late Ordovician–early Silurian in the Upper Yangtze area, South China. *J. Asian Earth Sci.* **2023**, *242*, 105496. [[CrossRef](#)]
10. Zhu, H.; Ju, Y.; Yang, M.; Huang, C.; Feng, H.; Qiao, P.; Ma, C.; Su, X.; Lu, Y.; Shi, E.; et al. Grain-scale petrographic evidence for distinguishing detrital and authigenic quartz in shale: How much of a role do they play for reservoir property and mechanical characteristic? *Energy* **2022**, *239*, 122176. [[CrossRef](#)]
11. Xu, H.; Zhou, W.; Hu, Q.; Yi, T.; Ke, J.; Zhao, A.; Lei, Z.; Yu, Y. Quartz types, silica sources and their implications for porosity evolution and rock mechanics in the Paleozoic Longmaxi Formation shale, Sichuan basin. *Mar. Petrol. Geol.* **2021**, *128*, 105036. [[CrossRef](#)]
12. Emmings, J.F.; Dowey, P.J.; Taylor, K.G.; Davies, S.J.; Vane, C.H.; Moss-Hayes, V.; Rushton, J.C. Origin and implications of early diagenetic quartz in the Mississippian Bowland Shale Formation, Craven Basin, UK. *Mar. Petrol. Geol.* **2020**, *120*, 104567. [[CrossRef](#)]
13. Kumar, S.; Ojha, K. Reaction kinetic, maturity, burial and thermal histories modelling of cambay shale source rocks, Cambay Basin, Western India. *J. Petrol. Sci. Eng.* **2021**, *202*, 108543. [[CrossRef](#)]
14. Dong, T.; He, S.; Chen, M.; Hou, Y.; Guo, X.; Wei, C.; Han, Y.; Yang, R. Quartz types and origins in the paleozoic Wufeng-Longmaxi Formations, Eastern Sichuan basin, China: Implications for porosity preservation in shale reservoirs. *Mar. Petrol. Geol.* **2019**, *106*, 62–73. [[CrossRef](#)]
15. Xiang-Rong, Y.; De-Tian, Y.; Xiao-Song, W.; Li-Wei, Z.; Bao, Z.; Han-Wen, X.; Yin, G.; Jie, H. Different formation mechanism of quartz in siliceous and argillaceous shales: A case study of Longmaxi Formation in South China. *Mar. Petrol. Geol.* **2018**, *94*, 80–94. [[CrossRef](#)]
16. Bain, D.C.; Duthie, D.M.L.; Thomson, C.M. Rates and processes of mineral weathering in soils developed on greywackes and shales in the Southern Uplands of Scotland. *Water Air Soil. Poll.* **1995**, *85*, 1069–1074. [[CrossRef](#)]
17. Rushton, A.W.A.; Stone, P.; Hughes, R.A. Biostratigraphical control of thrust models for the Southern Uplands of Scotland. *Trans. R. Soc. Edinb. Earth Sci.* **1995**, *86*, 137–152. [[CrossRef](#)]
18. Leggett, J.K.; Mckerrow, W.S.; Casey, D.M. The anatomy of a Lower Palaeozoic accretionary forearc: The Southern Uplands of Scotland. *Geol. Soc. Lond. Spec. Publ.* **1982**, *10*, 495–520. [[CrossRef](#)]
19. Imber, J.; Armstrong, H.; Clancy, S.; Daniels, S.; Herringshaw, L.; McCaffrey, K.; Rodrigues, J.; Trabucho-Alexandre, J.; Warren, C. Natural fractures in a United Kingdom shale reservoir analog, Cleveland Basin, northeast England. *AAPG Bull.* **2014**, *98*, 2411–2437. [[CrossRef](#)]

20. Wignall, P.B.; Macquaker, J.H.S.; Gawthorpe, R.L. Mudstone lithofacies in the Kimmeridge Clay Formation, Wessex Basin, southern England; implications for the origin and controls of the distribution of mudstones; discussion and reply. *J. Sediment. Res. Sect. A Sediment. Petrol. Process.* **1994**, *64*, 927–932. [[CrossRef](#)]
21. Lis-Śledziona, A.; Kaczmarczyk-Kuszpit, W. A Technique of Hydrocarbon Potential Evaluation in Low Resistivity Gas-Saturated Mudstone Horizons in Miocene Deposits, South Poland. *Energies* **2022**, *15*, 1890. [[CrossRef](#)]
22. Schultz, H.M.; Krüger, M.; Straaten, N.; Bechtel; Crabtree, S. *Biogenic Gas in the Cambrian-Ordovician Alum Shale (Denmark and Sweden)*; DGMK/ÖGEW-Frühjahrstagung, Fachbereich Aufsuchung und Gewinnung: Heidelberg, Germany, 2013; p. 2013.
23. Park, J.I. Geochemical Evidence for Fluid-Rock Interaction in the Ordovician Vinini Formation at Vinini Creek, Eureka County, Nevada. Master's Thesis, University of Nevada, Reno, Nevada, 2001.
24. Radtke, A.S.; Scheiner, B.J. Studies of hydrothermal gold deposition-(pt.) 1, carlin gold deposit, nevada, the role of carbonaceous materials in gold deposition. *Econ. Geol.* **1970**, *65*, 87–102. [[CrossRef](#)]
25. Slack, J.F.; McAleer, R.J.; Shanks, W.C.; Dumoulin, J.A. Diagenetic Barite-Pyrite-Wurtzite Formation and Redox Signatures in Triassic Mudstone, Brooks Range, Northern Alaska. *Chem. Geol.* **2021**, *585*, 120568. [[CrossRef](#)]
26. Soja, C.M. Silurian-bearing terranes of Alaska. *Spec. Pap. Geol. Soc. Am.* **2008**, *442*, 39–50.
27. Lacelle, D.; Doucet, A.; Clark, I.D.; Lauriol, B. Acid drainage generation and seasonal recycling in disturbed permafrost near Eagle Plains, northern Yukon Territory, Canada. *Chem. Geol.* **2007**, *243*, 157–177. [[CrossRef](#)]
28. Perry, D.G.; Klapper, G.; Lenz, A.C. Age of the Ogilvie Formation (Devonian), Northern Yukon: Based Primarily on the Occurrence of Brachiopods and Conodonts. *Can. J. Earth Sci.* **1974**, *11*, 1055–1097. [[CrossRef](#)]
29. Jackson, D.E.; Lenz, A.C. Zonation of Ordovician and Silurian Graptolites of Northern Yukon, Canada. *AAPG Bull.* **1962**, *46*, 30–45.
30. Li, M.; Luo, Q.; Chen, J.; Shi, S.; Yang, J.; Xu, X.; Qin, J.; Wang, Y.; Dong, Q. Redox conditions and nitrogen cycling in the Late Ordovician Yangtze Sea (South China). *Palaeogeogr. Palaeoclimatol. Palaeoecol.* **2021**, *567*, 110305. [[CrossRef](#)]
31. Xiao, D.; Cao, J.; Luo, B.; Tan, X.; Xiao, W.; He, Y.; Li, K. Neoproterozoic postglacial paleoenvironment and hydrocarbon potential: A review and new insights from the Doushantuo Formation Sichuan basin, China. *Earth-Sci. Rev.* **2021**, *212*, 103453. [[CrossRef](#)]
32. Zhou, T.; Cai, J.; Mou, S.; Zhao, Q.; Shi, Z.; Sun, S.; Guo, W.; Gao, J.; Cheng, F.; Wang, H. Influence of Low-Temperature Hydrothermal Events and Basement Fault System on Low-Resistivity Shale Reservoirs: A Case Study from the Upper Ordovician to Lower Silurian in the Sichuan basin, SW China. *Minerals* **2023**, *13*, 720. [[CrossRef](#)]
33. Zhou, T.; Zhu, Q.; Zhu, H.; Zhao, Q.; Shi, Z.; Zhao, S.; Zhang, C.; Qi, L.; Sun, S.; Zhang, Z.; et al. Relative Sea-Level Fluctuations during Rhuddanian–Aeronian Transition and Its Implication for Shale Gas Sweet Spot Forming: A Case Study of Luzhou Area in the Southern Sichuan basin, SW China. *J. Mar. Sci. Eng.* **2023**, *11*, 1788. [[CrossRef](#)]
34. Zhou, T.; Zhu, Q.; Zhu, H.; Zhao, Q.; Shi, Z.; Zhao, S.; Zhang, C.; Wang, S. DRAG: A Novel Method for Automatic Geological Boundary Recognition in Shale Strata Using Multi-Well Log Curves. *Processes* **2023**, *11*, 2998. [[CrossRef](#)]
35. Röhlich, P. Structure of the Prague Basin: The deformation diversity and its causes (the Czech Republic). *Bull. Geosci.* **2007**, *82*, 175–182. [[CrossRef](#)]
36. Budil, P.; Hörbinger, F.; Mencl, R. Lower Devonian dalmanitid trilobites of the Prague Basin (Czech Republic). *Earth Environ. Ence Trans. R. Soc. Edinb.* **2006**, *99*, 61–100. [[CrossRef](#)]
37. Prague, M.Z.C.R. Report on the State of Forests and Forestry in the Czech Republic. By December 31, 1999. 2000.
38. Bailey, A.H.E.; Henson, P. Variation of vertical stress in the onshore Canning basin, western Australia. *APPEA J.* **2019**, *59*, 364–382. [[CrossRef](#)]
39. Ben Clennell, M.; Josh, M.; Esteban, L.; Hill, D.; Woods, C.; McMullan, B.; Piane, C.D.; Schmid, S.; Verrall, M. The influence of pyrite on rock electrical properties: A case study from NW Australian gas reservoirs. In Proceedings of the SPWLA 51st Annual Logging Symposium, Perth, Australia, 19 June 2010.
40. Wei, C.; Dong, T.; He, Z.; He, S.; He, Q.; Yang, R.; Guo, X.; Hou, Y. Major, trace-elemental and sedimentological characterization of the upper Ordovician Wufeng-lower Silurian Longmaxi formations, Sichuan basin, south China: Insights into the effect of relative sea-level fluctuations on organic matter accumulation in shales. *Mar. Petrol. Geol.* **2021**, *126*, 104905. [[CrossRef](#)]
41. Xiao, B.; Liu, S.; Li, Z.; Ran, B.; Ye, Y.; Yang, D.; Li, J. Geochemical characteristics of marine shale in the Wufeng Formation–Longmaxi Formation in the northern Sichuan basin, South China and its implications for depositional controls on organic matter. *J. Petrol. Sci. Eng.* **2021**, *203*, 108618. [[CrossRef](#)]
42. Zhao, B.; Li, R.; Qin, X.; Wang, N.; Zhou, W.; Khaled, A.; Zhao, D.; Zhang, Y.; Wu, X.; Liu, Q. Geochemical characteristics and mechanism of organic matter accumulation of marine-continental transitional shale of the lower permian Shanxi Formation, southeastern Ordos Basin, north China. *J. Petrol. Sci. Eng.* **2021**, *205*, 108815. [[CrossRef](#)]
43. Hounslow, M.W.; Ratcliffe, K.T.; Harris, S.E.; Nawrocki, J.; Wójcik, K.; Montgomery, P.; Woodcock, N.H. The Telychian (early Silurian) oxygenation event in northern Europe: A geochemical and magnetic perspective. *Palaeogeogr. Palaeoclimatol. Palaeoecol.* **2021**, *567*, 110277. [[CrossRef](#)]
44. Wang, Y.; Cheng, H.; Hu, Q.; Liu, L.; Hao, L. Diagenesis and pore evolution for various lithofacies of the Wufeng-Longmaxi shale, southern Sichuan basin, China. *Mar. Petrol. Geol.* **2021**, *133*, 105251. [[CrossRef](#)]
45. Wood, D.A. Carbonate/siliciclastic lithofacies classification aided by well-log derivative, volatility and sequence boundary attributes combined with machine learning. *Earth Sci. Inf.* **2022**, *15*, 1699–1721. [[CrossRef](#)]

46. Wu, J.; Liang, C.; Yang, R.; Hu, Z.; Li, W.; Xie, J. The genetic relationship between paleoenvironment, mineral compositions and lithofacies in the Ordovician–Silurian Wufeng–Longmaxi sedimentary succession in the Sichuan basin, SW China. *J. Asian Earth Sci.* **2022**, *236*, 105334. [[CrossRef](#)]
47. Xie, H.; Liang, C.; Wu, J.; Cao, Y.; Han, Y.; Liu, Y.; Zhao, Z. Multiple geological events controlling rock types development: A case study of Wufeng–Longmaxi formation in southern Sichuan basin, China. *Geoenergy Sci. Eng.* **2023**, *227*, 211826. [[CrossRef](#)]
48. Wu, J.; Liang, C.; Yang, R.; Xie, J. The significance of organic matter–mineral associations in different lithofacies in the Wufeng and longmaxi shale–gas reservoirs in the Sichuan basin. *Mar. Petrol. Geol.* **2021**, *126*, 104866. [[CrossRef](#)]
49. Basilici, G.; Vidal, A.C. Alternating coarse- and fine-grained sedimentation in Precambrian deep-water ramp (Apiúna Formation, SE of Brazil): Tectonic and climate control or sea level variations? *Precambrian Res.* **2018**, *311*, 211–227. [[CrossRef](#)]
50. Cullers, R.L.; Podkovyrov, V.N. The source and origin of terrigenous sedimentary rocks in the Mesoproterozoic Ui group, southeastern Russia. *Precambrian Res.* **2002**, *117*, 157–183. [[CrossRef](#)]
51. Zhang, Z.; Guo, Y.; Zhao, D.; Zhang, J.; Zeng, C.; Li, Y. Control Model of Organic Shale Enrichment by Terrigenous Weathering in Wufeng Formation–Longmaxi Formation, Southeast Sichuan, China. *Minerals* **2023**, *13*, 761. [[CrossRef](#)]
52. Wu, L.; Lu, Y.; Jiang, S.; Liu, X.; Liu, Z.; Lu, Y. Relationship between the origin of organic-rich shale and geological events of the Upper Ordovician–Lower Silurian in the Upper Yangtze area. *Mar. Pet. Geol.* **2019**, *102*, 74–85. [[CrossRef](#)]
53. Shi, Z.; Zhou, T.; Wang, H.; Sun, S. Depositional Structures and Their Reservoir Characteristics in the Wufeng–Longmaxi Shale in Southern Sichuan basin, China. *Energies* **2022**, *15*, 1618. [[CrossRef](#)]
54. Shi, Z.; Zhou, T.; Guo, W.; Liang, P.; Cheng, F. Quantitative Paleogeographic Mapping and Sedimentary Microfacies Division in a Deep-water Marine Shale Shelf: Case study of Wufeng–Longmaxi shale, southern Sichuan basin, China. *Acta Sedimentol. Sin.* **2022**, *40*, 1728–1743.
55. Chen, X.; Fan, J.; Zhang, Y.; Wang, H.; Chan, Q.; Wang, W.; Liang, F.; Guo, W.; Zhao, Q. Subdivision and delineation of the wufeng and lungmachi black shales in the subsurface areas of the yangtze platform. *J. Stratigr.* **2015**, *39*, 351–358.
56. Pedersen, T.F.; Calvert, S.E. Anoxia vs. productivity: What controls the formation of organic- carbon-rich sediments and sedimentary rocks? *AAPG Bull.* **1990**, *74*, 454–466.
57. Crusius, J.; Calvert, S.; Pedersen, T.; Sage, D. Rhenium and molybdenum enrichments in sediments as indicators of oxic, suboxic and sulfidic conditions of deposition. *Earth Planet. Sc. Lett.* **1996**, *145*, 65–78. [[CrossRef](#)]
58. Nesbitt, H.W.; Young, G.M. Early proterozoic climates and plate motions inferred from major element chemistry of lutites. *Nature* **1982**, *299*, 715–717. [[CrossRef](#)]
59. Ocularid, S.G.; Rimmer, S.M.; Conder, J.A. Redox conditions associated with organic carbon accumulation in the Late Devonian New Albany Shale, west-central Kentucky, Illinois Basin. *Int. J. Coal Geol.* **2017**, *190*, 42–55. [[CrossRef](#)]
60. Mohialdeen, I.M.J.; Hakimi, M.H. Geochemical characterisation of Tithonian–Berriasian Chia Gara organic-rich rocks in northern Iraq with an emphasis on organic matter enrichment and the relationship to the bioproductivity and anoxia conditions. *J. Asian Earth Sci.* **2016**, *116*, 181–197. [[CrossRef](#)]
61. Algeo, T.J.; Maynard, J.B. Trace-element behavior and redox facies in core shales of Upper Pennsylvanian Kansas-type cyclothems. *Chem. Geol.* **2004**, *206*, 289–318. [[CrossRef](#)]
62. Algeo, T.J.; Tribouillard, N. Environmental analysis of paleoceanographic systems based on molybdenum–uranium covariation. *Chem. Geol.* **2009**, *268*, 211–225. [[CrossRef](#)]
63. Kumar, D.; Rajesh, K.; Mondal, S.; Warsi, T.; Rangarajan, R. Groundwater exploration in limestone–shale–quartzite terrain through 2D electrical resistivity tomography in Tadipatri, Anantapur district, Andhra Pradesh. *J. Earth Syst. Sci.* **2020**, *129*, 71. [[CrossRef](#)]
64. Cai, Q.; Hu, M.; Kane, O.I.; Li, M.; Zhang, B.; Hu, Z.; Deng, Q.; Xing, N. Cyclic variations in paleoenvironment and organic matter accumulation of the Upper Ordovician–Lower Silurian black shale in the Middle Yangtze Region, South China: Implications for tectonic setting, paleoclimate, and sea-level change. *Mar. Petrol. Geol.* **2022**, *136*, 105477. [[CrossRef](#)]
65. Dong, T.; Harris, N.; Ayranci, K. Relative sea-level cycles and organic matter accumulation in shales of the Middle and Upper Devonian Horn River Group, northeastern British Columbia, Canada: Insights into sediment flux, redox conditions, and bioproductivity. *GSA Bull.* **2018**, *130*, 859–880. [[CrossRef](#)]
66. Ge, X.; Mou, C.; Yu, Q.; Liu, W.; Men, X.; He, J. The geochemistry of the sedimentary rocks from the Huadi No. 1 well in the Wufeng–Longmaxi formations (Upper Ordovician–Lower Silurian), South China, with implications for paleoweathering, provenance, tectonic setting and paleoclimate. *Mar. Petrol. Geol.* **2019**, *103*, 646–660. [[CrossRef](#)]
67. Gao, Z.; Xiong, S.; Wei, L. The new multistage water adsorption model of Longmaxi Formation shale considering the spatial configuration relationship between organic matter and clay minerals. *Petrol. Sci.* **2022**, *19*, 1950–1963. [[CrossRef](#)]
68. Xie, W.; Chen, S.; Vandeginste, V.; Yu, Z.; Wang, H.; Wang, M. Review of the Effect of Diagenetic Evolution of Shale Reservoir on the Pore Structure and Adsorption Capacity of Clay Minerals. *Energy Fuel* **2022**, *36*, 4728–4745. [[CrossRef](#)]
69. Wang, R.; Ding, W.; Zhang, Y.; Wang, Z.; Wang, X.; He, J.; Zeng, W.; Dai, P. Analysis of developmental characteristics and dominant factors of fractures in Lower Cambrian marine shale reservoirs: A case study of Niutitang formation in Cen’gong block, southern China. *J. Petrol. Sci. Eng.* **2016**, *138*, 31–49. [[CrossRef](#)]
70. Bornemann, A.; Pirkenseer, C.M.; De Deckker, P.; Speijer, R.P. Oxygen and carbon isotope fractionation of marine ostracod calcite from the eastern Mediterranean Sea. *Chem. Geol.* **2012**, *310–311*, 114–125. [[CrossRef](#)]

71. Leng, M.J.; Jones, M.D.; Frogley, M.R.; Eastwood, W.J.; Kendrick, C.P.; Roberts, C.N. Detrital carbonate influences on bulk oxygen and carbon isotope composition of lacustrine sediments from the Mediterranean. *Glob. Planet. Chang.* **2010**, *71*, 175–182. [[CrossRef](#)]
72. Luan, G.; Azmy, K.; Meyer, R.; Olanipekun, B.; Dong, C. Origin of carbonate cements in Ben Nevis sandstones of Jeanne d'Arc Basin: Insights from geochemistry. *Mar. Petrol. Geol.* **2023**, *148*, 106033. [[CrossRef](#)]
73. Lei, Z.; Xu, H.; Jiang, T.; Yan, D. In-situ major and rare earth elements constraint on the growth mechanism of calcite cement in shallow marine sandstone: An example from the Donghe sandstones, Tabei uplift, Tarim Basin, NW China. *Mar. Petrol. Geol.* **2021**, *134*, 105325. [[CrossRef](#)]
74. Schieber, J.; Shao, X. Detecting detrital carbonate in shale successions-Relevance for evaluation of depositional setting and sequence stratigraphic interpretation. *Mar. Petrol. Geol.* **2021**, *130*, 105130. [[CrossRef](#)]
75. Ardakani, O.H.; Sanei, H.; Jackson, S.E.; Al-Aasm, I.S. Geochemistry of dolomite fluorescence in response to thermal maturity: An example from Upper Ordovician Utica Shale of southern Québec, Canada. *Int. J. Coal Geol.* **2020**, *231*, 103593. [[CrossRef](#)]
76. Hu, X.; Müller, I.A.; Zhao, A.; Ziegler, M.; Chen, Q.; Han, L.; Shi, Z. Clumped isotope thermometry reveals diagenetic origin of the dolomite layer within late Ordovician black shale of the Guanyinqiao Bed (SW China). *Chem. Geol.* **2022**, *588*, 120641. [[CrossRef](#)]
77. Wu, A.; Cao, J.; Zhang, J.; Wu, T.; Wang, Y. Origin of microbial–hydrothermal bedded dolomites in the Permian Lucaogou Formation lacustrine shales, Junggar Basin, NW China. *Sediment. Geol.* **2022**, *440*, 106260. [[CrossRef](#)]
78. Riechelmann, S.; Mavromatis, V.; Buhl, D.; Dietzel, M.; Immenhauser, A. Controls on formation and alteration of early diagenetic dolomite: A multi-proxy  $\delta^{44}/^{40}\text{Ca}$ ,  $\delta^{26}\text{Mg}$ ,  $\delta^{18}\text{O}$  and  $\delta^{13}\text{C}$  approach. *Geochim. Cosmochim. Acta* **2020**, *283*, 167–183. [[CrossRef](#)]

**Disclaimer/Publisher's Note:** The statements, opinions and data contained in all publications are solely those of the individual author(s) and contributor(s) and not of MDPI and/or the editor(s). MDPI and/or the editor(s) disclaim responsibility for any injury to people or property resulting from any ideas, methods, instructions or products referred to in the content.